EDITORIAL BOARD

PATRON-IN-CHIEF

EDITOR-IN-CHIEF

R. Ahmad, Institute of Physics,
Government College University, Lahore-54000, PAKISTAN
E-mail: jnsm@gcu.edu.pk
http://gcu.edu.pk/NSMJournal.htm

A. Shahbaz (Editor)

Saif Ullah (Editor)

Sajjad Ahmad (Associate Editor)

ADVISORY BOARD

Panel of Foreign Advisors

H. M. Srivastava
Department of Mathematics and Statics,
University of Victoria, British Columbia, Canada.

J. Meng
School of Physics,
Peking University, Beijing, P. R.
China.

Dumitru Vieru
Department of Theoretical
Mechanics,
Technical University, Gheorghe
Asachi of Iasi, Romania.

K. P. Shum
Department of Mathematics,
Hong Kong University, China
(SAR)

N. Tsintsadze
Institute of Physics,
Institute of Physics, Tbitsi, Georgia.

Cemil Tunc
Department of Mathematics,
Yuzuncu Yil University, Turkey.

Jisheng Pan
Institute of Material Research and
Engineering (IMRE), Singapore

T. Kaladze
Vekua Institute of Applied
Mathematics,
Tbilisi State University, Georgia.

PS. Lee
School of Material Sciences and
Engineering,
NTU Singapore.

Panel of Local Advisors

M. Zakaullah
Department of Physics,
Quaid-i-Azam University, Islamabad.

Najeeb Alam Khan
Department of Mathematical Sciences,
University of Karachi.

N. A. D. Khattak
Department of Physics,
Gomal University, D.I. Khan.

M. Tariq Rahim
National University of Computer & Emerging Sciences (FAST),
Peshawar.

Saeed Aslam
Department of Mathematics,
Abdul Wali Khan University, Mardan.

M. S. Iqbal
Department of Chemistry,
F. C. College (a charted University), Lahore.

Arshad Majid Mirza
Department of Physics,
Quaid-i-Azam University, Islamabad.

Shahid Mahmood
Department of Physics,
University of Karachi.

Annual Subscription

Pakistan: Rs 250 | Foreign Countries: US$ 40 | Overseas Air Mail Charges: US$ 10

The Journal is published bi-annually
In April and October

Published by:
Riaz Ahmad, Government College University, Lahore, Pakistan.
Printed at:

CONTENTS

PK ISSN 0022- 2941; CODEN JNSMAC
Vol. 56, (2016) PP 01-05

DEPENDENCE OF MORPHOLOGY CHARACTERISTICS ON SUBSTRATE TEMPARATURES FOR PARA-SEXIPHENYL THIN FILMS GROWN BY HOT WALL EPITAXY USING MUSCOVITE MICA

K. REHMAN[1*] AND HELMUT SITTER[1]

[1] Institute of Semiconductor and Solid State Physics, Johannes Kepler University, Linz, Austria
[1*]Govt Postgraduate College for Women, Wahdat Road Lahore, Pakistan

ABSTRACT: The characteristic self-assembling nature of para sexi-phenyl (PSP) into nano-fibres of high crystalline form is making this material gain importance in the world of OFET's and OLED's. In order to achieve better parallel alignment of such organic nano-needles as (PSP) on muscovite mica, finding the optimum parameters and applying them in a controlled manner during growth needs further research. Further a thermodynamically ideal setup for growth of optimized needle morphology is needed which is provided by Hot Wall Epitaxy (HWE) which is used here as we present experimental data carried out on such lines as explained above.

Keywords: Para sexi-phenyl, Thin films, Hot Wall Epitaxy, Substrate temperature

1. INTRODUCTION

In the past, new devices have been devised by combining high macroscopic and microscopic order with nano-structures where these ideal molecular assemblies are the building blocks [1, 2]. By this progress, the importance of self assembled nano-structures in the realm of nano-technology has been established [3]. The research has intensified regarding optimum growth of one or two dimensional nano-structures as the challenges remain [4].

The growth of phenylenes on muscovite mica is epitaxial result in self assembling into parallel aligned nano-fibers [5-7] provides polarized emission of a high degree [8] and has led to applications like lasers [9-11], waveguides [12-15] and frequency doublers [16]. Hence the prerequisite for optimizing the achievable length of the organic nano-fibres is the ability to form parallel needles [17]. For this purpose the combination of muscovite mica with phenylenes is outstanding [18, 19].

In this article we present a study into the effect of different parameters during growth on the final needle morphology of para sexi-phenyl on muscovite mica grown in the hot wall epitaxial system.

As shown in the Fig 1 (a) and (b), the epitaxial growth of PSP on muscovite mica surface produces a characteristic morphology. We have selected the phenylene PSP on the substrate most suitable for uni-directional needle growth; muscovite mica. The random arrangement of needles on phlogopite mica points towards external influence like electric field required to make an attempt to get order restricting our present study to muscovite mica. The experimental approach comprising of atomic force microscopy gives accurate values for all three morphology parameters namely length, width and height of the nano-needles.

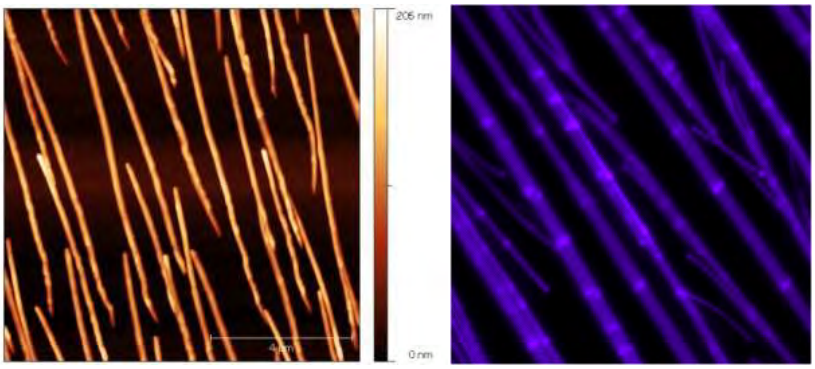

(a) **(b)**

Fig 1: (a) The AFM image of needle orientations of para sexi-phenyl on muscovite mica and (b) shows an optical microscope image of para sexi-phenyl needles at a cleavage step of muscovite mica.

The understanding of these parameters governing the morphology pattern of PSP nano-needles is a recognized fundamental of the research in nano-technology and the results yielded by our work are a part of the efforts being made in this direction.

2. METHODS

Thin Film Deposition

The organic source material of PSP used for the growth experiments was purchased from TCI and was purified by thermal sublimation. It was then filled in a quartz tube and placed in the HWE reactor. The 15x15 mm^2 muscovite mica substrates purchased from Segliwa GMBH were freshly cleaved and immediately transferred to the HWE chamber working at a vacuum of $6x10^{-6}$ mbar. A 30 minutes in situ pre-heating at the substrate deposition temperature was carried out to rid the substrate surface of any adsorbed species before the deposition of the organic molecules. The growth time was 90 minutes keeping a source temperature of 200°C and a wall temperature of 220°C while the substrate temperature was 120, 140, 160, 170, 180, 190, 200, and 210°C for length and width statistics of the nano-needles while

additional four samples grown at substrate temperatures of 220, 230, 240 and 250°C were used for height statistics.

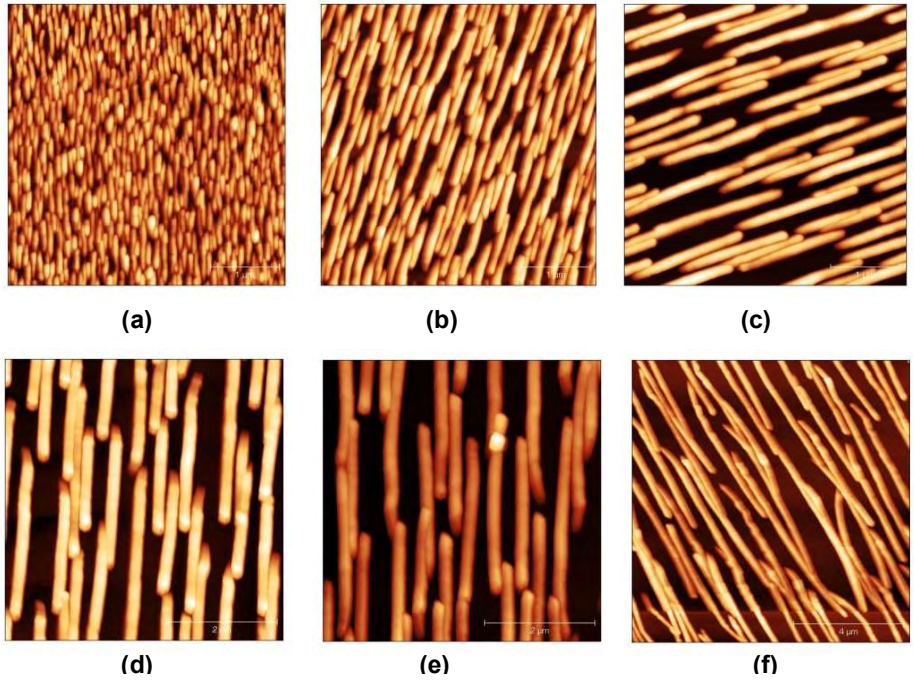

Fig 2: AFM images of PSP needles grown at substrate temperatures of (a) 120°C, (b) 140°C, (c) 160°C, (d) 170°C, (e) 180°C and (f) 190°C. The image size is (a), (b), (c) 4x4 μm^2 (d), (e) 5x5 μm^2 and (f) 10x10 μm^2.

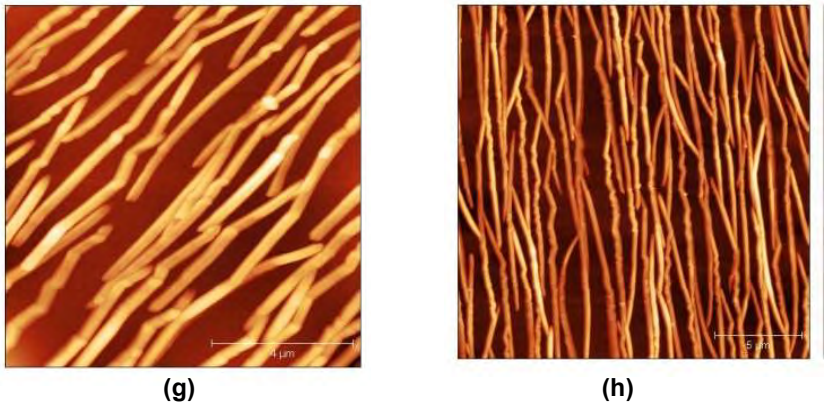

Fig 3: AFM images of PSP needles grown at substrate temperatures of (g) 200°C and (h) 210°C. The image size is (g) 10x10 μm^2 and (h) 20x20 μm^2

3. RESULTS

Morphology and Structure

Here we focus on the understanding of needle growth on muscovite mica to prove the importance of growth system and growth parameters on the final morphology of the needles.

The lengths and widths of the needles were measured by AFM scans while for the heights of the needles the fluorescence images were used in addition to AFM scans. The figure 2 and 3 shows the AFM scans for the first eights samples. Figure 4 shows the confocal images of the next samples in the series.

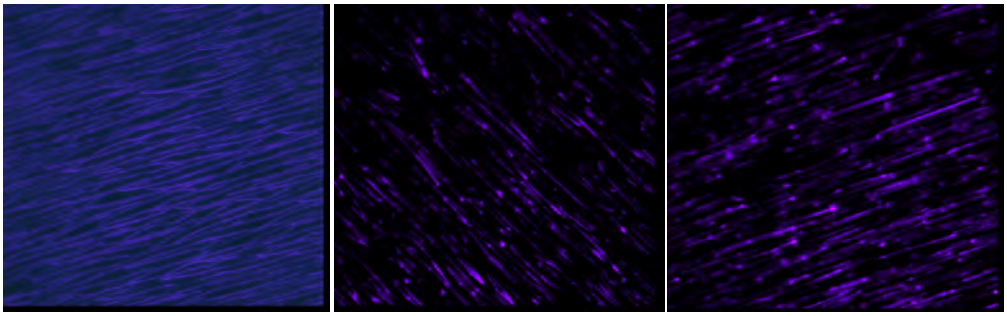

(a) 50 µm **(b)** 40 µm **(c)** 40 µm

Fig 4: Confocal images of samples grown at substrate temperature of (a) 220°C, (b) 230°C, (c) 240°C.

4. DISCUSSION

It is observed that the needle lengths, widths and heights increase linearly with increase in substrate temperature. However at an elevated substrate temperature of 260°C all needle growth stops due to the loss of temperature gradient between the source and substrate in the hot wall reactor. The needles first decrease in number at substrate temperature of 250°C and then disappear at 260°C.

5. SUMMARY AND CONCLUSION

Accurate measurements of morphology characteristics were enabled by the combination of AFM and fluorescence microscopy for the experimental data. Controlled substrate temperatures can lead to an ideal achievable lengths and widths of PSP nano-needles which are few of the pre-requisites for highly polarized emission by PSP nano-needles in the blue spectral range in several optical devices fabrication.

REFERENCES

1. A. P. H. J. Schenning and E. W. Meijer, Chem. Commun., 26 (2005) 3245-3258.
2. Q. Niu, Y. Zhou, L. Wang, J. Peng, J. Pei and Y. Cao, Adv. Mater., 20 (2008) 964-969.
3. E. Gazit, Chem. Soc. Rev., 36 (2007) 1263-1269.
4. M. Schiek, F. Balzer, K. Al-Shamery, A. Lützen and H.-G. Rubahn, Soft Matter, 4 (2008) 277-285.
5. A. Andreev, H. Sitter, N. S. Sariciftci, C. J. Brabec, G. Springholz, P. Hinterdorfer, H. Plank, R. Resel, A. Thierry and B. Lotz, Thin Solid Films, 403 (2002) 444-448.

6. R. Resel, T. Haber, O. Lengyel, H. Sitter, F. Balzer, and H.-G. Rubahn, Surf. Interface Anal., 41 (2009) 764-770.
7. F. Balzer and H.-G. Rubahn, Surf. Sci., 548 (2004) 170-182.
8. A. Andreev, G. Matt, C. J. Brabec, H. Sitter, D. Badt, H. Seyringer and N. S. Sariciftci, Adv. Mater., 12 (2000) 629.
9. F. Quochi, J. Opt., 12 (2010) 024003.
10. A. Andreev, F. Quochi, F. Cordella, A. Mura, G. Bongiovanni, and H. Sitter, J. Appl. Phys., 99 (2006) 034305.
11. F. Quochi, F. Cordella, A. Mura, G. Bongiovanni, F. Balzer, and H.-G. Rubahn, Appl. Phys. Lett., 88 (2006) 041106.
12. F. Balzer, V. Bordo, A. Simonsen and H.-G. Rubahn, Phys. Rev- B, 67 (2003) 115408.
13. H. Yanagi, A. Yoshiki, S. Hotta and S. Kobayashi, J. Appl. Phys., 96 (2004) 4240-4244.
14. V. Bordo, Phys. Rev. B, 73 (2006) 205177.
15. V. S. Volkov, S. I. Bozhevolnyi, V. G. Bordo and H.-G. Rubahn, J. Microsc., 215 (2004) 241-244.
16. J. Brewer, M. Schiek, A. Ltzen, K. Al-Shamery and H.-G. Rubahn, Nano Lett., 6 (2006) 2656-2659.
17. C. Simbrunner, D. Nabok, G. Hernandez-Sosa, M. Oehzelt, T. Djuric, R. Resel, L. Romaner, P. Puschnig, C. Ambrosch-Draxl, I. Salzmann, G. Schwabegger, I. Watzinger and H. Sitter, J. Am. Chem. Soc., 133 (2011) 3056-3062.
18. M. Schiek, F. Balzer, K. Al-Shamery, A. Lützen and H.-G. Rubahn, Soft Matter, 4 (2007) 277-285.
19. C. Simbrunner, F. Quochi, G. Hernandez-Sosa, M. Oehzelt, R. Resel, G. Hesser, M. Arndt, M. Saba, A. Mura, G. Bongiovanni and H. Sitter, ACS Nano, 4 (2010) 6244-6250.

PK ISSN 0022- 2941; CODEN JNSMAC
Vol. 56, (2016) PP 06-10

STUDY OF MORPHOLOGY PARAMETERS OF LENGTH, WIDTH AND HEIGHT WITH VARYING GROWTH PARAMETERS FOR PARA-SEXIPHENYL THIN FILMS ON MUSCOVITE MICA USING HOT WALL EPITAXY

K. REHMAN[1*] AND HELMUT SITTER[1]

[1] Institute of Semiconductor and Solid State Physics, Johannes Kepler University, Linz, Austria.
[1*]Govt Postgraduate College for Women, Wahdat Road Lahore, Pakistan

ABSTRACT

One of the key factors governing the performance of many optical and electrical devices has been found to be the self-assembling of organic nano-structures. The research is still continuing as by finding the optimum parameters to be applied during growth of certain organic nano-needles as para-sexiphenyl (PSP) on muscovite mica promises their better parallel alignment. Here we present experimental data and deduced results carried out by using a thermodynamically ideal setup, Hot Wall Epitaxy (HWE) for optimized needle parameters in addition to a comparison with a similar study differing in the growth system.

1. INTRODUCTION

Using muscovite mica as substrate, the growth of phenylenes has been seen to be epitaxial, resulting in their self-assembling into parallel aligned nano fibres [1-3]. The resulting polarized emission is of a high degree [4] and has led to applications like lasers [5-7], waveguides [8-11] and frequency doublers [12]. Hence for reaching the optimum achievable length of the organic nano fibres, the first step is the ability to form parallel needles [13]. The best combination serving this purpose is of muscovite mica with phenylenes [14, 15].

In this article we present a study into the effect of different parameters during growth on the final needle morphology of para-sexiphenyl on muscovite mica grown in the hot wall epitaxial system. We have selected the phenylene PSP on the substrate most suitable for uni-directional needle growth; muscovite mica. The experimental approach comprising mostly of atomic force microscopy gives accurate values for all three morphology parameters namely length, width and height of the nano needles.

The results of our findings have been compared to those obtained by others using molecular beam epitaxy as their technique for growth [16].

Past researches indicate self-assembled nano structures to be of huge importance in nano technology [17].Using these ideal molecular assemblies as building blocks, new

devices have been designed [18] by the combination of nano-structures with high microscopic as well as macroscopic order [19]. The optimum development of one or two dimensional nano structures still being a challenge [20] has resulted in extensive research.

The understanding of these parameters governing the morphology pattern of PSP nano needles is a recognized fundament of the research in nano-technology and the results yielded by our work are a part of the efforts being made in this direction.

2. METHODS

Thin Film Deposition

The organic source material of PSP used for the growth experiments was purchased from TCI and was purified by thermal sublimation. It was then filled in a quartz tube and placed in the HWE reactor. The 15x15mm^2 muscovite mica substrates purchased from Segliwa GMBH were freshly cleaved and immediately transferred to the HWE chamber working at a vacuum of 6x10^{-6} mbar. A 30 minutes in situ pre-heating at the substrate deposition temperature was carried out to rid the substrate surface of any adsorbed species before the deposition of the organic molecules. The growth time was 90 minutes keeping a source temperature of 200°C and a wall temperature of 220°C while the substrate temperature was 120, 140, 160, 170, 180, 190, 200, and 210°C for length and width statistics of the nano needles while an additional four samples grown at substrate temperatures of 220, 230, 240 and 250°C were used for height statistics.

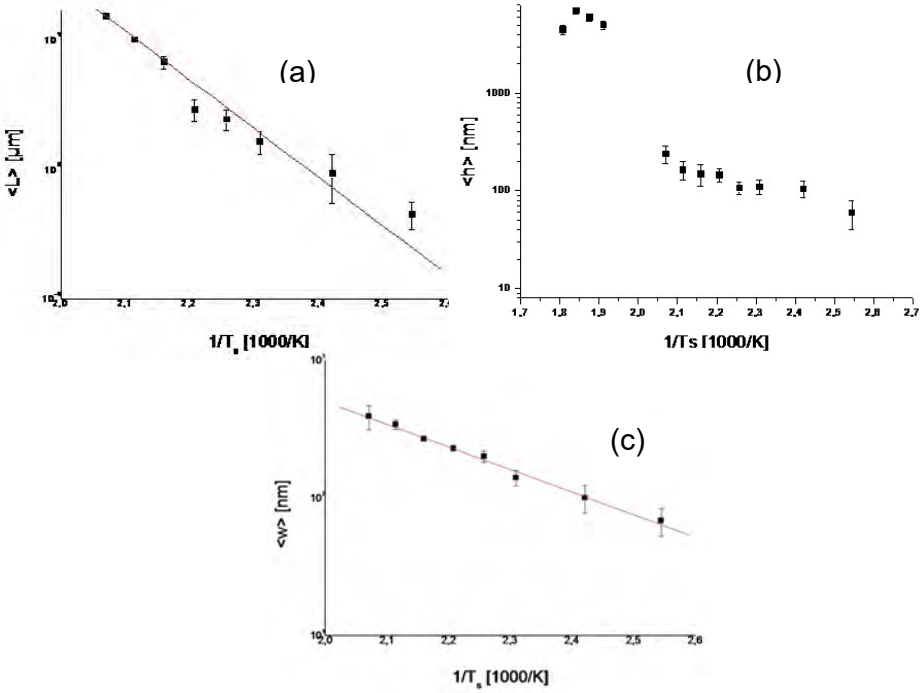

Figure 4: Arrhenius plots for the mean (a) fibre- length <L>, (b) fibre-height <h> and (c) fibre-width <w>.

3. MORPHOLOGY STUDIES

The optical images were obtained using a commercially available Nikon Type 115 digital camera. Atomic force microscopy (AFM) images of the deposited organic films were conducted using a Digital Instruments Dimension 3100 in the tapping mode, while the AFM characterization was carried out on areas of 10x10 μm^2 and 20x20 μm^2 with a SiC tip.

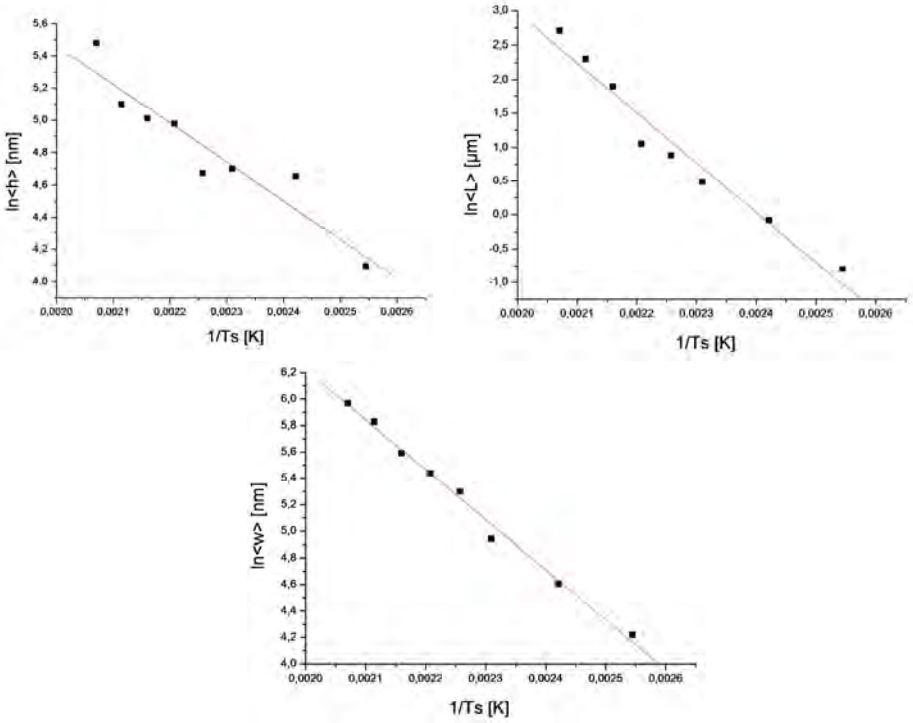

Figure 5: Log natural versus inverse temperature plots for (a) h, (b) L and (c) w.

4. RESULTS

Morphology and Structure

Here we focus on the understanding of needle growth on muscovite mica to prove the importance of growth system and growth parameters on the final morphology of the needles.

The lengths and widths of the needles were measured by AFM scans while for the heights of the needles the fluorescence images were used in addition to AFM scans.

In order to calculate the activation energies for L, h and w the slopes of the plots shown in figure 5 were used.

5. SUMMARY AND CONCLUSION

The combination of AFM and fluorescence microscopy for the experimental data yield accurate measurements of morphology characteristics. We found that all activation energies for the length, width and height of the needles are drastically affected by the substrate temperature. Controlling the temperature of the substrate can lead to ideal

achievable lengths and widths of PSP nano needles which are of extreme importance in several optical devices fabrication.

REFERENCES

1. A. Andreev, H. Sitter, N. S. Sariciftci, C. J. Brabec, G. Springholz, P. Hinterdorfer, H. Plank, R. Resel, A. Thierry and B. Lotz, Thin Solid Films, 403 (2002) 444-448.
2. R. Resel, T. Haber, O. Lengyel, H. Sitter, F. Balzer, and H.-G. Rubahn, Surf. Interface Anal., 41 (2009) 764-770.
3. F. Balzer and H.-G. Rubahn, Surf. Sci., 548 (2004) 170-182.
4. A. Andreev, G. Matt, C. J. Brabec, H. Sitter, D. Badt, H. Seyringer and N. S. Sariciftci, Adv. Mater., 12 (2000) 629.
5. F. Quochi, J. Opt., 12 (2010) 024003.
6. A. Andreev, F. Quochi, F. Cordella, A. Mura, G. Bongiovanni, and H. Sitter, J. Appl. Phys., 99 (2006) 034305.
7. F. Quochi, F. Cordella, A. Mura, G. Bongiovanni, F. Balzer, and H.-G. Rubahn, Appl. Phys. Lett., 88 (2006) 041106.
8. F. Balzer, V. Bordo, A. Simonsen and H.-G. Rubahn, Phys. Rev- B, 67 (2003) 115408.
9. H. Yanagi, A. Yoshiki, S. Hotta and S. Kobayashi, J. Appl. Phys., 96 (2004) 4240-4244.
10. V. Bordo, Phys. Rev. B, 73 (2006) 205177.
11. V. S. Volkov, S. I. Bozhevolnyi, V. G. Bordo and H.-G. Rubahn, J. Microsc., 215 (2004) 241-244.
12. J. Brewer, M. Schiek, A. Ltzen, K. Al-Shamery and H.-G. Rubahn, Nano Lett., 6 (2006) 2656-2659.
13. C. Simbrunner, D. Nabok, G. Hernandez-Sosa, M. Oehzelt, T. Djuric, R. Resel, L. Romaner, P. Puschnig, C. Ambrosch-Draxl, I. Salzmann, G. Schwabegger, I. Watzinger and H. Sitter, J. Am. Chem. Soc., 133 (2011) 3056-3062.
14. M. Schiek, F. Balzer, K. Al-Shamery, A. Lützen and H.-G. Rubahn, Soft Matter, 4 (2007) 277-285.
15. C. Simbrunner, F. Quochi, G. Hernandez-Sosa, M. Oehzelt, R. Resel, G. Hesser, M. Arndt, M. Saba, A. Mura, G. Bongiovanni and H. Sitter, ACS Nano, 4 (2010) 6244-6250.
16. L. Kankate, F. Balzer, H. Niehus and H.-G. Rubahn, J. Chem. Phys., 128 (2008) 084709.
17. E. Gazit, Chem. Soc. Rev., 36 (2007) 1263-1269.
18. Q. Niu, Y. Zhou, L. Wang, J. Peng, J. Pei and Y. Cao, Adv. Mater., 20 (2008) 964-969.

19. A. P. H. J. Schenning and E. W. Meijer, Chem. Commun., 26 (2005) 3245-3258.
20. M. Schiek, F. Balzer, K. Al-Shamery, A. Lützen and H.-G. Rubahn, Soft Matter, 4 (2008) 277-285.

PK ISSN 0022- 2941; CODEN JNSMAC
Vol. 56, (2016) PP 11-15

STUDY OF GROWTH RATE OF RUBERENE ON INORGANIC DIELECTRICS FOR UNDERSTANDING THE INFLUENCE OF SUBSTRATE TEMPERATURES ON GROWTH AS COMPARED TO SOURCE TEMPERATURES

K. REHMAN*[1] AND H. SITTER[1]

[1]Institute of Semiconductor and Solid State Physics, Johannes Kepler University, Linz, Austria.
*[1]Govt Postgraduate College for Women, Wahdat Road Lahore, Pakistan

ABSTRACT

Due to its remarkable carrier transport capabilities, the hydrocarbon rubrene is a prominent candidate for the active semiconducting layer in organic thin film transistors. Hole mobilities as high as 20 cm^2 V^{-1} s^{-1} reported for single crystals at room temperature have recently attracted much attention towards this material.

Here we report on the preparation of thin films of rubrene on two dielectric materials mica and SiO_2 at same substrate temperatures resulting in nominal film thicknesses starting from submonolayer. To study the molecular growth dynamics of rubrene films on these substrates, we characterized the films by atomic force microscopy and reported the dependence of growth more on source temperatures than on substrate temperatures.

1. INTRODUCTION

In single crystal organic transistors the aromatic hydrocarbon rubrene has been reported to have the highest charge carrier mobility of 20 cm^2/Vs [1-7], ensuring its place as a promising candidate for organic thin film electronics. Good results have been seen for single crystal of rubrene however not for rubrene thin films [8-15]. When efforts were made to grow rubrene thin films with crystalline morphology, the results were mostly amorphous films with small polycrystalline areas namely spherulites [16-18]. In order to fully understand the reasons behind these drastically diverse morphologies, an in depth study of the different stages of rubrene thin film growth is desirable. Attempts have been made to study the initial stage of island formation [17-30] and the following stage of coalescence and thin film formation followed by the nucleation of spherulites [30]. In order to best understand the morphology of rubrene thin films it is essential to study the initial stages of growth of rubrene on different substrates. Here we have attempted the same using inorganic substrates of mica and SiO_2 in order to study the dependence of growth of rubrene on substrate temperatures.

2. EXPERIMENTAL METHODS

Rubrene obtained from Aldrich with a purity of more than 98% was further purified by thermal sublimation. The deposition of rubrene was carried out on freshly cleaved mica (001) and freshly cleaned SiO_2 wafer substrates by hot wall epitaxy in vacuum of 10^{-6} mbar at substrate temperatures of 90°C and 120°C while the source temperature was at 180°C. Morphology assessment was done by obtaining AFM scans from Digital Instruments Dimension 3100 in the tapping mode. Figure 1 shows the AFM scans of rubrene grown on muscovite mica and SiO_2 substrates.

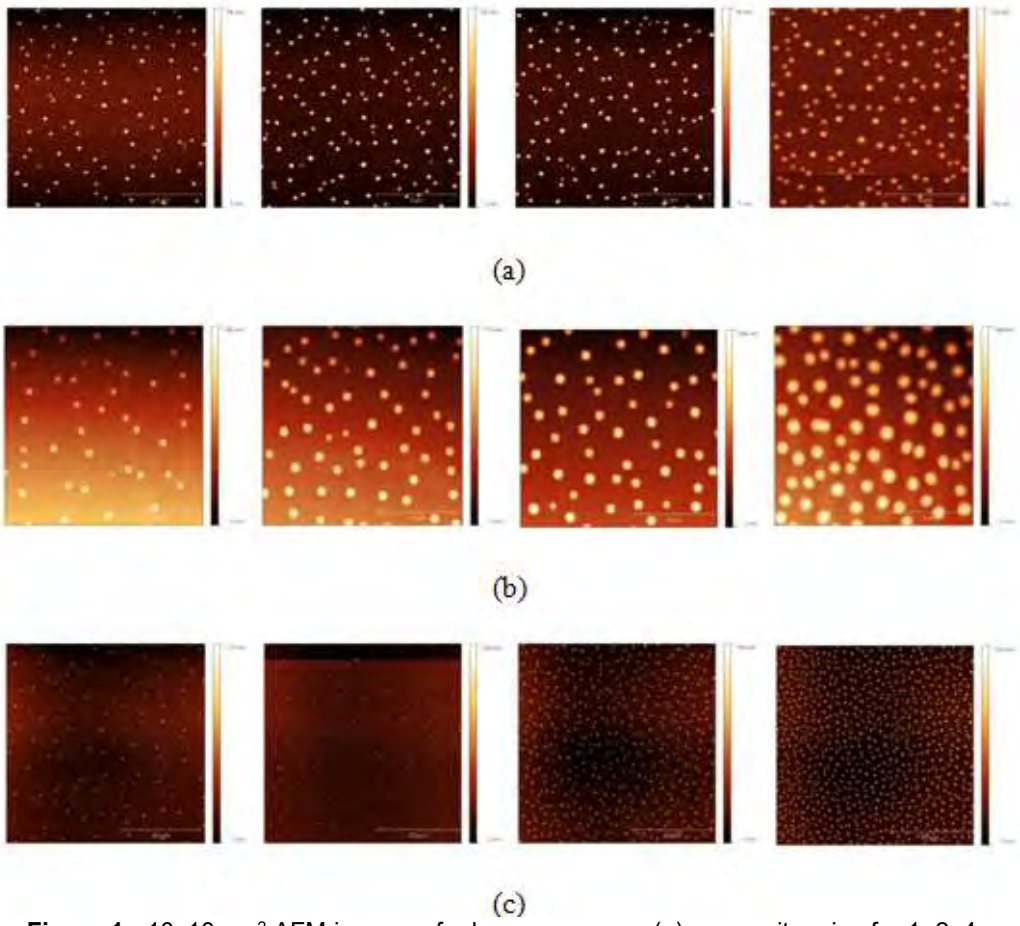

Figure 1: 10x10 μm^2 AFM images of rubrene grown on (a) muscovite mica for 1, 2, 4 and 8 minutes (left to right) at T_{sub}= 90°C, (b) muscovite mica for 1, 2, 4 and 8 minutes (left to right) at T_{sub}= 120°C and (c) 50x50 μm^2 SiO_2 for 0.5, 1, 2 and 4 minutes (left to right) at T_{sub}= 120°C.

3. RESULTS

The growth rate in each series of samples was found by plotting the NFT versus the time of growth and the plots are shown in figure 2 which gives the corresponding growth rate in monolayers (ML) per minute as 0.37 ML/min, 0.47 ML/min and 0.38 ML/min for the first (mica), second (mica) and third (SiO_2) series of samples respectively whose AFM scans are given in Figure 1. It can be seen that the increase

of substrate temperature in the first two series of samples increases the growth rate but not by a high value. It implies that the growth rate dependence is more on the source temperature than on the substrate temperature.

Figure 2: Plot of nominal film thickness versus the time of growth on (a) muscovite

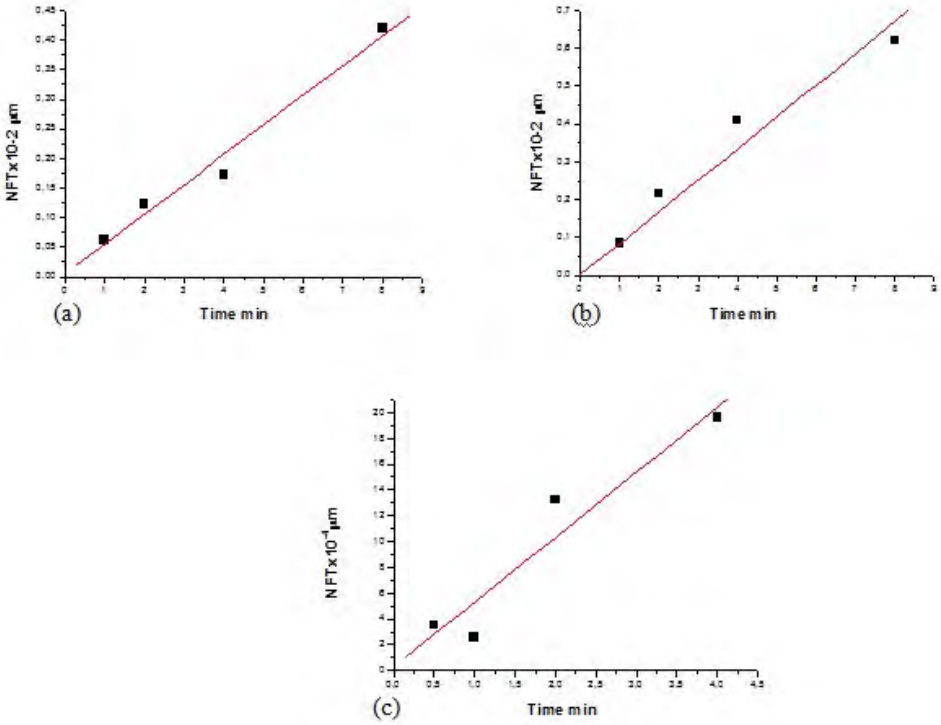

mica at T_{sub}= 90°C, (b) muscovite mica at T_{sub}= 120°C and (c) SiO_2 at T_{sub}= 120°C. Although the investigations carried out to find the nominal film thickness for substrate temperatures of 90°C and 120°C on muscovite mica, similar results for higher substrate temperatures were observed.

4. SUMMARY AND CONCLUSION

We have investigated the nucleation stage of rubrene layers grown by Hot-Wall-Epitaxy on different substrates at different temperatures. Keeping the impingement rate constant for all investigations, the increase of the substrate temperature, as well as the change of the substrate material, did not significantly change the growth rate. That means, that the growth process is dominated by the source temperature.

REFERENCES

1. V. Podzorov, E. Menard, A. Borissov, V. Kiryukhin, J. A. Rogers and M. E. Gershenson, Phys. Rev. Lett., 93 (2004) 8.
2. F. Balzer, M. Schiek, A. Lützen and K. Al-Shamery, Proc. SPIE, 6470 (2007) 647006.
3. Y. Luo, M. Brun, P. Rannou and B.Grevin, Phys. stat. sol., 204 (2007) 1851.

4. S. Seo, B. Park and Paul G. Evans, Appl. Phys. Lett., 88 (2006) 232114.
5. M. C. Scharber, D. Wuhlbacher, M. Koppe, P. Denk, C. Waldauf, A. J. Heeger and C. L. Brabec, Adv. Mater., 18 (6) (2006) 789-794.
6. J. L. Bredas, J. E. Norton, J. Cornil and V. Coropceanu, Acc. Chem. Res., 42 (11) (2009) 1691-1699.
7. C. W. Schlenker and M. E. Thompson, Topics in Current Chemistry, 312 (2011) 175-212.
8. S. W. Park, J. M. Hwang, J. M. Choi, D. K. Hwang, M. S. Oh, J. H. Kim and S. Im, Appl. Phys. Lett., 90 (15) (2007) 153512.
9. S. W. Park, S. H. Jeong, J. M. Choi, J. M. Hwang, J. H. Kim and S. Im, Appl. Phys. Lett. 91 (2007) 033506.
10. C. H. Hsu, J. Deng, C. R. Staddon and P. H. Beton, Appl. Phys. Lett., 91 (2007) 193505.
11. V. Podzorov, S. E. Sysoev, E. Loginova, V. M. Pudalov and M. E. Gershenson, Appl. Phys. Lett., 82, (2003) 1739.
12. V. C. Sundar, J. Zaumseil, V. Podzorov, E. Menard, R. L. Willett, T. Someya, M. E. Gershenson and J. A. Rogers, Science, 303 (2004) 1644.
13. C. Goldmann, S. Haas, C. Krellner, K. P. Pernstich, D. J. Gundlach and B. Batlogg, J. Appl. Phys., 96 (2004) 2080.
14. E. Menard, V. Podzorov, S. H. Hur, A. Gaur, M. E. Gershenson and J. A. Rogers, Adv. Mater., 16 (2004) 2097.
15. J. Takeya, M. Yamagishi, Y. Tominari, R. Hirahara, Y. Nakazawa, T. Nishikawa, T. Kawase, T. Shimoda and S. Ogawa, Appl. Phys. Lett., 90 (2007) 102120.
16. H. Klauk, M. Halik, U. Zschieschang, G. Schmid, W. Radik and W. Weber, J. Appl. Phys., 92 (2002) 5259.
17. C. D. Sheraw, L. Zhou, J. R. Huang, D. J. Gundlach, T. N. Jackson, M. G. Kane, G. Hill, M. S. Hammond, J. Campi, B. K. Greening, J. Francl and J. West, Appl. Phys. Lett., 80 (2002) 1088.
18. D. Käfer, L. Ruppel, G. Witte and Ch. Wöll, Phys. Rev. Lett., 95 (2005) 166602.
19. M. J. Campione, Phys. Chem. C, 112 (2008) 16178.
20. M. Haemori, J. Yamaguchi, S. Yaginuma, K. Itaka and H. Koinuma, Jpn. J. Appl. Phys., 44 (2005) 740.
21. C. H. Hsu, J. Deng, C. R. Staddon and P. H. Beton, Appl. Phys. Lett., 91 (2007) 193505.
22. D. Käfer and G. Witte, Phys. Chem. Chem. Phys. 7 (2005) 2850.
23. Y. Chen and I. Shih, Appl. Phys. Lett., 75 (2009) 2039.
24. Y. Luo, M. Brun, P. Rannou and B. Grevin, Phys. Stat. Sol. (a), 204 (2007) 1851.
25. P. R. Ribič and G. J. Bratina, Phys. Chem. C., 111 (2007) 18558.

26. S. Kowarik, A. Gerlach, S. Sellner, F. Schreiber, J. Pflaum, L. Cavalcanti and O. Konovalov, Phys. Chem. Chem. Phys., 8 (2006) 1834.
27. G. Hlawacek, Sh. M. Abd Al-Baqi, X. M. He, H. Sitter and C. Teichert, Springer Proc. Phys., 129 (2009) 55.
28. L. Granasy, T. Pusztai, T. Borzsonyi, J. A. Warren and J. F. Douglas, Nat. Mater., 3 (2004) 645.
29. M. Brinkmann, S. Graff and F. Biscarini, Phys. Rev. B, 66 (2002) 165430.
30. Y. Kato, S. Iba, R. Teramoto, T. Sekitani, T. Someya, H. Kawaguchi and T. Sakurrai, Appl. Phys. Lett., 84 (2004) 3789.
31. B. Stadlober, U. Hass, H. Maresch and A. Haase, Physical Review B, 74 (2006) 165302.

PK ISSN 0022- 2941; CODEN JNSMAC
Vol. 56, (2016) PP 16-31

INVESTIGATIONS OF STEADY ISOTHERMAL TWO DIMENSIONAL BLOOD FLOW FOR AN OLDROYD-B FLUID THROUGH THE STENOSED CHANNEL

A. A. MIRZA[a,1], A. M. SIDDIQUI[b]

a. Department of Mathematics, COMSATS Institute of Information Technology, Park Road, Chak Shahzad, Islamabad, Pakistan.
b. Department of Mathematics, Pennsylvania State University, York Campus, 1031 Edgecomb Avenue, York, PA 17403, USA.

azharali_mirza1@yahoo.com

ABSTRACT

In the current analysis the hemodynamics behavior of blood flow in a stenosed channel is investigated. Blood is assumed to be isothermal Oldroyd-B fluid which is independent of time. The governing equations for an Oldroyd-B fluid are transformed into stream function formulation and resultant highly non-linear compatibility equation is solved by regular perturbation technique by considering δ, which is the ratio of semi width of the channel to the length of channel, as a small parameter. In this analysis analytical and numerical solutions through graphs are presented for stream lines, wall shear stress, separation and reattachment points, pressure gradient and velocity distribution. At the end conclusion and deduction are made of the current results to the existing results in the literature and finds good agreement.

Keywords: Oldroyd-B fluid, wall shear stress, separation and reattachment points

1. INTRODUCTION

It is well known that the deposit of cholesterol and proliferation of connective tissue may be responsible for the abnormal growths in the lumen of the artery. The actual cause is not known exactly but its effect on cardiovascular system can easily be understood by studying the blood flow in its vicinity. Many authors studied the behavior of blood in the stenosed artery and they considered the blood as a Newtonian and non-Newtonian fluid, the most earliest and basic paper about blood flow is of Young [1], in which he suggested that the boundary irregularities can be an important factor in the development and progression of arterial disease. Forrester and Young [2] presented the analytical solution of Newtonian fluid for the axisymmetric, steady, incompressible flow and consider the mild stenosis for the flow of blood both theoretically and experimentally in the converging and diverging tube. Lee and Fung [3] solved the problem numerically. Morgan and Young [4] presented the approximate analytical solution of axisymmetric, steady flow, which is applicable to both mild and severe stenosis by using an integral method; basically they presented the extension of [2]. K. Haldar [5] investigated the blood flow through an axisymmetric stenosed

artery and stenosis is of cosine shape. Chow et al. [6] presented solution for symmetric channel with sinusoidal wall variation. One of the practical application of blood flowing is through membrane oxygenator with irregular wall surface. Many authors studied the behavior of blood as a Non-Newtonian fluid due to its suspension of cells at low shear rate. Shukla et al. [7] presented the analysis by considering blood as Non-Newtonian fluid and study the effect of stenosis on the resistance to flow and wall shear stress in an artery. Mishra and Shit [8] considered the Herschel-Bulkley equation to represent the non-Newtonian character of blood. Haldar [9] discussed the effect of the shape of stenosis on the resistance of blood flow through an artery with mild local narrowing. Cheng and Michel [10] discussed the blood as steady and pulsatile physiological flows. Azhar *et al.* [11] discussed steady two-dimensional Navier-Stokes equations for the flow of blood in an axisymmetric artery having a constriction. They found that an increase in the height of the constriction increases the velocity of blood, wall shear stress, pressure and temperature. Azhar *et al.* [12] presents the comparison of two analytical methods i,e. Adomian decomposition method and regular perturbation method and conclude that the Adomian decomposition method is efficient, reliable, easily computable and provides a fast convergent series.

In the present analysis, the blood is assumed to be Oldroyd-B fluid between the two parallel plates and the governing equations are presented in terms of stream function as a compatibility equation. The analytical solutions are found by using regular perturbation technique and numerically through graphs the effects of stream lines, wall shear stress, points of separation and reattachment, velocity distribution and pressure gradient are presented numerically through graphs.

2. GOVERNING EQUATIONS

The basic equations which govern the flow of an incompressible Oldroyd-B fluid neglecting thermal effect are continuity equation and conservation of momentum defined as

$$\tilde{\vec{\nabla}} \cdot \tilde{\vec{V}} = 0, \tag{1}$$

$$\rho \frac{d\tilde{\vec{V}}}{dt} = \tilde{\vec{\nabla}} \cdot \tilde{\tau} + \rho \tilde{b} \tag{2}$$

where $\tilde{\vec{V}} = \left(\tilde{u}\left(\tilde{x}, \tilde{y}\right), \tilde{v}\left(\tilde{x}, \tilde{y}\right), 0\right)$ and ρ are the velocity vector and constant density of fluid respectively, $\tilde{b}$ the body force per unit mass, $\tilde{\tau}$ is Cauchy stress tensor and $\frac{d}{dt}$ the material time derivative given by

$$\frac{d(\cdot)}{dt} = \frac{\partial(\cdot)}{\partial \tilde{t}} + \tilde{u} \frac{\partial(\cdot)}{\partial \tilde{x}} + \tilde{v} \frac{\partial(\cdot)}{\partial \tilde{y}} \tag{3}$$

The constitutive equation for Cauchy stress tensor $\widetilde{\tau}$ for Oldroyd-B fluid is defined as

$$\widetilde{\tau} = -p\widetilde{I} + \widetilde{S}, \tag{4}$$

where two dimensional $\widetilde{S}$ will be

$$\begin{bmatrix} \widetilde{S}_{\widetilde{x}\widetilde{x}} & \widetilde{S}_{\widetilde{x}\widetilde{y}} \\ \widetilde{S}_{\widetilde{y}\widetilde{x}} & \widetilde{S}_{\widetilde{y}\widetilde{y}} \end{bmatrix}$$

and p is dynamic pressure, $\widetilde{I}$ the identity tensor and the constitutive equation for extra stress tensor $\widetilde{S}$ is given below

$$\widetilde{S} + \lambda_1 \frac{D\widetilde{S}}{Dt} = \mu\left(\widetilde{A}_1 + \lambda_2 \frac{D\widetilde{A}_1}{Dt}\right) \tag{5}$$

in which

$$\frac{D\widetilde{S}}{Dt} = \frac{d\widetilde{S}}{dt} - \widetilde{S}\left(\widetilde{\nabla}\widetilde{V}\right) - \left(\widetilde{S}\left(\widetilde{\nabla}\widetilde{V}\right)\right)^{\mathrm{T}} \tag{6}$$

$$\frac{D\widetilde{A}_1}{Dt} = \frac{d\widetilde{A}_1}{dt} - \widetilde{A}_1\left(\widetilde{\nabla}\widetilde{V}\right) - \left(\widetilde{A}_1\left(\widetilde{\nabla}\widetilde{V}\right)\right)^{\mathrm{T}} \tag{7}$$

where μ is the coefficient of viscosity, $\frac{D}{Dt}$ convective time derivative, λ_1, λ_2 are relaxation and retardation time and $\widetilde{A}_1$ is first Rivlin-Ericksen tensor defined as

$$\widetilde{A}_1 = \vec{\widetilde{\nabla}}\widetilde{V} + (\vec{\widetilde{\nabla}}\widetilde{V})^{\mathrm{T}}$$

where superscript T denotes the transpose of tensor.

3. PROBLEM FORMULATION

Consider the steady, incompressible blood flow through the channel of infinite length having stenosis of length $l_o/2$. The coordinate system is chosen in such a way that the channel lies in the $\widetilde{x}\widetilde{y} - plane$ and $\widetilde{x} - axis$ coincide with the center line in the direction of flow and $\widetilde{y} - axis$ is perpendicular to $\widetilde{x} - axis$.

The boundary of the stenosed region is chosen of the form [5] as

$$\begin{aligned} h(\widetilde{x}) &= h_o - \frac{\lambda}{2}\left(1 + \cos\left(\frac{4\pi\widetilde{x}}{l_o}\right)\right), && -\frac{l_o}{4} < \widetilde{x} < \frac{l_o}{4}, \\ &= h_o && \text{otherwise}, \end{aligned} \tag{8}$$

where $h(\widetilde{x})$ is the variable height of the stenosis, $2h_o$ the width of the unobstructed channel, λ the maximum height of stenosis.

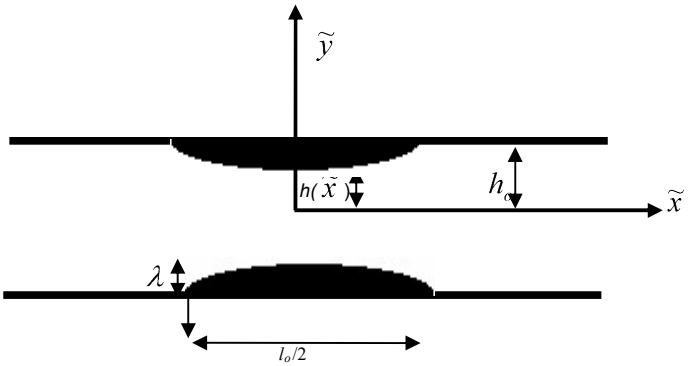

Figure 1: Geometry of the problem.

Introducing the dimensionless quantities as follows

$$x=\frac{\tilde{x}}{l_o},\ y=\frac{\tilde{y}}{h_o},\quad u=\frac{\tilde{u}}{u_o},\ v=\frac{\tilde{v}}{u_o},\quad p=\frac{h_o^2}{\mu u_o l_o}\tilde{p} \tag{9}$$

where u_o is the characteristic velocity. Boundary conditions according to the geometry of problem in dimensionless form are

$$\begin{aligned} &u=v=0, && at && y=f,\\ &\frac{\partial u}{\partial y}=0, && at && y=0,\\ &\int_0^f u\,dy=-\frac{1}{2}. \end{aligned} \tag{10}$$

The first two conditions are the no slip, third is symmetry and last is flow per unit depth of the parallel plates.

Dimensionless form of the boundary profile is

$$\begin{aligned} f(x)&=1-\frac{\varepsilon}{2}\left(1+\cos(4\pi x)\right), && -\frac{1}{4}<x<\frac{1}{4}\\ &=1 && \text{otherwise} \end{aligned} \tag{11}$$

where ε is the maximum height of constriction. Now introducing the stream functions to transform the nonlinear governing equations in one variable as

$$u=\frac{\partial \psi}{\partial y},\quad v=-\delta\frac{\partial \psi}{\partial x} \tag{12}$$

which satisfy the continuity equation identically and component form of momentum and constitutive equation in terms of stream function becomes

$$\frac{\partial q}{\partial x}-\mathrm{Re}\,\delta\left(\frac{\partial \psi}{\partial x}\right)\nabla^2\psi=\delta\frac{\partial S_{xx}}{\partial x}+\frac{\partial S_{yx}}{\partial y} \tag{13}$$

$$\frac{\partial q}{\partial y} - \mathrm{Re}\,\delta\left(\frac{\partial \psi}{\partial y}\right)\nabla^2\psi = \delta\left(\frac{\partial S_{yy}}{\partial y} + \delta\frac{\partial S_{yx}}{\partial x}\right) \tag{14}$$

$$S_{xx} + \alpha\delta\left\{\frac{\partial(\psi, S_{xx})}{\partial(y,\, x)} - 2\left(S_{xx}\frac{\partial^2\psi}{\partial x\partial y} - \delta S_{yx}\frac{\partial^2\psi}{\partial x^2}\right)\right\}$$
$$= 2\delta\left\{\frac{\partial^2\psi}{\partial x\partial y} + \beta\delta^2\left\{\left(\delta\frac{\partial\psi}{\partial y}\frac{\partial}{\partial x} - \frac{\partial\psi}{\partial x}\frac{\partial}{\partial y}\right)\frac{\partial^2\psi}{\partial x\partial y} - 2\left(\frac{\partial^2\psi}{\partial x\partial y}\right)^2 + \frac{\partial^2\psi}{\partial x^2}\left(\frac{\partial^2\psi}{\partial y^2} - \delta^2\left(\frac{\partial^2\psi}{\partial x^2}\right)^2\right)\right\}\right\} \tag{15}$$

$$S_{yx} + \alpha\left\{\delta\frac{\partial(\psi, S_{yx})}{\partial(y,\, x)} - \left(S_{xx}\frac{\partial^2\psi}{\partial y^2} + \delta^2 S_{yy}\frac{\partial^2\psi}{\partial x^2}\right)\right\}$$
$$= \frac{\partial^2\psi}{\partial y^2} - \delta^2\frac{\partial^2\psi}{\partial x^2} + \beta\delta\left\{\left(\delta\frac{\partial\psi}{\partial y}\frac{\partial}{\partial x} - \frac{\partial\psi}{\partial x}\frac{\partial}{\partial y}\right)\left(\frac{\partial^2\psi}{\partial y^2} - \delta^2\frac{\partial^2\psi}{\partial x^2}\right) - 2\frac{\partial^2\psi}{\partial x\partial y}\frac{\partial^2\psi}{\partial y^2}\left(1 - \delta^2\frac{\partial^2\psi}{\partial x^2}\right)\right\} \tag{16}$$

$$S_{yy} + \alpha\left\{\delta\frac{\partial(\psi, S_{yy})}{\partial(y,\, x)} - 2\left(S_{yx}\frac{\partial^2\psi}{\partial y^2} - \delta S_{yy}\frac{\partial^2\psi}{\partial x\partial y}\right)\right\}$$
$$= -2\delta\left\{\frac{\partial^2\psi}{\partial x\partial y} - 2\beta\left\{\delta^2\frac{\partial\left(\psi, \dfrac{\partial^2\psi}{\partial x\partial y}\right)}{\partial(y,\, x)} + \left(\frac{\partial^2\psi}{\partial y^2}\right)^2 - \delta^2\frac{\partial^2\psi}{\partial x^2}\frac{\partial^2\psi}{\partial y^2} + 2\delta^2\left(\frac{\partial^2\psi}{\partial x\partial y}\right)^2\right\}\right\} \tag{17}$$

where q is the modified pressure. Eliminating the modified pressure from (13) and (14), the compatibility equation in terms of stream function is obtained as

$$\mathrm{Re}\,\delta\frac{\partial\left(\psi, \nabla^2\psi\right)}{\partial(y,\, x)} = \delta\frac{\partial^2}{\partial x\partial y}\left(S_{xx} - S_{yy}\right) + \left(\frac{\partial^2}{\partial y^2} - \delta^2\frac{\partial^2}{\partial x^2}\right)S_{yx} \tag{18}$$

where $q = p + \dfrac{\mathrm{Re}\,\delta}{2}\left(u^2 + v^2\right)$ and $\nabla^2\psi = \delta^2\dfrac{\partial^2\psi}{\partial x^2} + \dfrac{\partial^2\psi}{\partial y^2}$ (19)

Boundary conditions in terms of stream functions are reduces as

$$\begin{aligned} &\frac{\partial\psi}{\partial y} = 0, \qquad \psi = -\frac{1}{2} \qquad at \qquad y = f, \\ &\frac{\partial^2\psi}{\partial y^2} = 0, \qquad \psi = 0, \qquad at \qquad y = 0, \end{aligned} \tag{20}$$

where $\alpha = \dfrac{\lambda_1 u_o}{h_o}$, $\beta = \dfrac{\lambda_2 u_o}{h_o}$, $\delta = \dfrac{h_o}{l_o}$, $\mathrm{Re} = \dfrac{u_o h_o}{\nu}$, $\mathrm{f} = \dfrac{h(\tilde{x})}{h_o}$, $\varepsilon = \dfrac{\lambda}{h_o}$

(21)

Now our task is to find the components of extra stress tensor and solve the above nonlinear equations along with the boundary conditions.

4. SOLUTION

It is observed that the compatibility equation is highly non-linear and exact solution is very difficult to find. Regular perturbation technique is applied to find the analytical

solution by considering δ as a small parameter, which is the requirement of the concerned method, as

$$\begin{aligned}\psi &= \psi_o + \delta\psi_1 + \delta^2\psi_2 + \cdots \\ S_{xx} &= S_{xx}^{(0)} + \delta S_{xx}^{(1)} + \delta^2 S_{xx}^{(2)} + \cdots, \\ S_{yx} &= S_{yx}^{(0)} + \delta S_{yx}^{(1)} + \delta^2 S_{yx}^{(2)} + \cdots, \\ S_{yy} &= S_{yy}^{(0)} + \delta S_{yy}^{(1)} + \delta^2 S_{yy}^{(2)} + \cdots.\end{aligned} \tag{22}$$

Using equation (22) in the above system of equations and considering one by one the zeroth, first and second order system as follows.

4.1. Zeroth order system

Comparing the coefficients of δ^0 on both sides of (15) - (20), we get

$$S_{xx}^{(0)} = 0 \tag{23}$$

$$S_{yx}^{(0)} = \frac{\partial^2 \psi_o}{\partial y^2} \tag{24}$$

$$S_{yy}^{(0)} = 2(\alpha - \beta)\left(\frac{\partial^2 \psi_o}{\partial y^2}\right)^2 \tag{25}$$

$$\frac{\partial^2 S_{yx}^{(0)}}{\partial y^2} = 0 \tag{26}$$

The boundary conditions for the zeroth order system in terms of stream function are

$$\begin{aligned}&\frac{\partial \psi_o}{\partial y} = 0, \qquad \psi_o = -\frac{1}{2} \qquad at \qquad y = f, \\ &\frac{\partial^2 \psi_o}{\partial y^2} = 0, \qquad \psi_o = 0, \qquad at \qquad y = 0,\end{aligned} \tag{27}$$

Solution of equations (24) and (26) along with the boundary conditions (27) is given in the form

$$\psi_o = \frac{\eta}{4}\left(\eta^2 - 3\right), \qquad \text{where} \qquad \eta = \frac{y}{f} \tag{28}$$

and

$$S_{yx}^{(0)} = \frac{3\eta}{2f^2}. \tag{29}$$

It is observed that ψ_o is independent of relaxation and retardation time parameters, which corresponds to Newtonian fluid.

4.2. First order system and solution

Equating the coefficients of δ on both sides of (15) - (20), we obtain

$$S_{xx}^{(1)} = 2\frac{\partial^2 \psi_o}{\partial x \partial y}, \tag{30}$$

$$S_{yx}^{(1)} + \alpha\left\{\frac{\partial(\psi_o, S_{yx}^{(o)})}{\partial(y,\, x)} - S_{xx}^{(o)}\frac{\partial^2 \psi_o}{\partial y^2}\right\} = \frac{\partial^2 \psi_1}{\partial y^2} + \beta\left\{\frac{\partial\left(\psi_o, \frac{\partial^2 \psi_o}{\partial y^2}\right)}{\partial(y,\, x)} - 2\frac{\partial^2 \psi_o}{\partial x \partial y}\frac{\partial^2 \psi_o}{\partial y^2}\right\} \tag{31}$$

$$S_{yy}^{(1)} + \alpha\left\{\frac{\partial(\psi_o, S_{yy}^{(o)})}{\partial(y,\, x)} - 2\left(S_{yx}^{(1)}\frac{\partial^2 \psi_o}{\partial y^2} + S_{yx}^{(o)}\frac{\partial^2 \psi_1}{\partial y^2} - S_{yy}^{(o)}\frac{\partial^2 \psi_o}{\partial x \partial y}\right)\right\} = -2\frac{\partial^2 \psi_o}{\partial x \partial y} - 4\beta\frac{\partial^2 \psi_o}{\partial y^2}\frac{\partial^2 \psi_1}{\partial y^2} \tag{32}$$

$$\mathrm{Re}\frac{\partial}{\partial y}\left(\frac{\partial(\psi_o, S_{yy}^{(o)})}{\partial(y,\, x)}\right) = \frac{\partial^2 S_{yx}^{(1)}}{\partial y^2} - \frac{\partial^2 S_{yy}^{(o)}}{\partial x \partial y} \tag{33}$$

along with the boundary conditions in terms of stream functions are

$$\begin{aligned} &\frac{\partial \psi_1}{\partial y} = 0, \qquad \psi_1 = -\frac{1}{2} \qquad at \qquad y = f, \\ &\frac{\partial^2 \psi_1}{\partial y^2} = 0, \qquad \psi_1 = 0, \qquad at \qquad y = 0, \end{aligned} \tag{34}$$

The solution of equations (31) and (33) along with boundary conditions (34) is given by

$$\psi_1 = -\frac{3\eta f'}{1120 f^2}\left(\eta^2 - 1\right)^2\left\{\mathrm{Re}\, f^2\left(\eta^2 - 5\right) + 84(\alpha - \beta)\right\} \tag{35}$$

and

$$S_{yx}^{(1)} = -\frac{3\eta f'}{560 f^6}\left\{\mathrm{Re}\, f^4\left(21\eta^4 - 70\eta^2 + 33\right) + 24 f^2(\alpha - \beta)\left(70\eta^2 - 21\right)\right\} \tag{36}$$

It is observed that equation (35) reduces to first order solution for viscous fluid by setting $\alpha = \beta = 0$.

4.3. Second order system

Second order system is obtained by comparing the coefficients of δ^2 on both sides of (15) - (20). The solution of concerned equations along with the respective boundary conditions is obtained as

$$\begin{aligned} \psi_2 = {} & \frac{\eta(\eta-1)^2}{3449600 f^4}\Big[\, 5544(\eta+1)^2\{\, 3\beta^2\{\, \left(26 f'^2 - 5 f f''\right)\eta^2 - \left(34 f'^2 - 13 f f''\right)\,\} + 2\alpha^2\{\, 5\left(89 f'^2 - 5 f f''\right)\eta^2 \\ & + 2\left(347 f'^2 - 39 f f''\right)\,\} - \alpha\beta\{\, 5\left(256 f'^2 + 25 f f''\right)\eta^2 + \left(1286 f'^2 + 117 f f''\right)\,\}\,\} - 924(\alpha-\beta) f^2 \\ & \{\, 140\alpha\{\, 3\left(7 f'^2 - f f''\right)\eta^3 + 6\left(7 f'^2 - f f''\right)\eta^2 + \left(19 f'^2 - 2 f f''\right)(2\eta+1)\,\}\mathrm{Re}(\eta+1)^2\{\, 5\left(7 f'^2 - 2 f f''\right)\eta^4 \\ & - 2\left(79 f'^2 + 23 f f''\right)\eta^2 + 9\left(11 f'^2 + 2 f f''\right)\,\}\,\} + (\eta+1)^2 f^4\{\, 258720\left(f f'' - 4 f'^2\right) + \mathrm{Re}^2\{\, \left(98 f'^2 - 35 f f''\right)\eta^6 \\ & - \left(959 f'^2 - 315 f f''\right)\eta^4 + \left(24727 f'^2 - 853 f f''\right)\eta^2 - \left(2875 f'^2 - 1213 f f''\right)\,\}\,\}\,\Big]. \end{aligned} \tag{37}$$

and

$$S_{yx}^{(2)}=\frac{\eta}{1724800f^{6}}\Big[\ 44352\{\ \alpha\beta\{\ 420\left(ff''-10f'^{2}\right)\eta^{4}-245\left(ff''-8f'^{2}\right)\eta^{2}-6\left(9ff''-107f'^{2}\right)\}$$
$$+6\beta^{2}\{\ 35\left(10f'^{2}-ff''\right)\eta^{4}-\left(35\eta^{2}-3\right)\left(8f'^{2}-ff''\right)\}+\alpha^{2}\{\ 210\left(10f'^{2}-ff''\right)\eta^{4}-35\left(8f'^{2}-ff''\right)\eta^{2}$$
$$-6\left(131f'^{2}-12ff''\right)\}\ \}+2772(\alpha-\beta)f^{2}\{\ 700\alpha\{\ 3\left(ff''-7f'^{2}\right)\eta^{3}-2\left(ff''-5f'^{2}\right)\eta+3f'^{2}\ \}$$
$$+\mathrm{Re}\{\ 105\left(8f'^{2}-ff''\right)\eta^{6}-7\left(428f'^{2}-61ff''\right)\eta^{4}+5\left(232f'^{2}-79ff''\right)\eta^{2}-\left(356f'^{2}-73ff''\right)\}\ \}\qquad(38)$$
$$+f^{4}\{\ 258720\{\ 15\left(ff''-4f'^{2}\right)\eta^{2}+\left(11ff''-34f'^{2}\right)\}+\mathrm{Re}^{2}\{\ 5\left(1078f'^{2}-385ff''\right)\eta^{8}$$
$$-13860\left(3f'^{2}-ff''\right)\eta^{6}+2\left(47124f'^{2}-15939ff''\right)\eta^{4}-20\left(4389f'^{2}-1617ff''\right)\eta^{2}$$
$$+\left(24666f'^{2}-9837ff''\right)\eta^{2}\ \}\ \}\ \Big]$$

The solution in equation (37) is more general; one can obtain the result for second order viscous fluid by setting $\alpha=\beta=0$. It is found that by setting $\alpha=0$, the solution for Jeffrey fluid could be obtained and if $\beta=0$ results for Maxwell fluid could be observed.

4.4. Pressure Distribution

To find the pressure gradient substituting $p=p_o+\delta p_1+\delta^2 p_2+\cdots$, in equations (13)-(14) and making use of (19) and (22), we obtained system of equations for pressure gradient as follows.

4.4.1. Zeroth order pressure and solution

Comparing the coefficients of δ^0, we get

$$\frac{\partial p_o}{\partial x}=\frac{\partial S_{yx}^{(o)}}{\partial y}\qquad(39)$$

$$\frac{\partial p_o}{\partial y}=0\qquad(40)$$

Solution of above two equations by using $p=\int_0^z\frac{\partial p}{\partial z}dz\ +\ \int_0^r\frac{\partial p}{\partial r}dr\qquad(41)$

is $$p_o=-\frac{3}{32\pi\left(\varepsilon-1\right)^{2}}\left[\begin{array}{l}\dfrac{1}{\sqrt{\varepsilon-1}}\left(3\varepsilon^{2}-8\varepsilon+8\right)\tanh^{-1}\left(\dfrac{\tan 2\pi x}{\sqrt{\varepsilon-1}}\right)\\+\dfrac{f'}{8\pi f^{2}}\left\{16\left(\varepsilon-1\right)-3\varepsilon^{2}-3\varepsilon\left(\varepsilon-2\right)\cos\left(2\pi x\right)\right\}\end{array}\right]\qquad(42)$$

which is independent of time relaxation (α) and time retardation (β). The zeroth order pressure for Oldroyd-B fluid is similar to zeroth order pressure for viscous and second grade fluid.

4.4.2. First order pressure and solution

Equating the coefficients of δ, we obtain

$$\frac{\partial p_1}{\partial x}+\mathrm{Re}\left(\frac{\partial\psi_o}{\partial y}\frac{\partial^2\psi_o}{\partial x\partial y}-\frac{\partial\psi_o}{\partial x}\frac{\partial^2\psi_o}{\partial y^2}\right)=\frac{\partial S_{xx}^{(o)}}{\partial x}+\frac{\partial S_{yx}^{(1)}}{\partial y}\qquad(43)$$

$$\frac{\partial p_1}{\partial y} = \frac{\partial S_{yy}^{(o)}}{\partial y} \tag{44}$$

The solution of above equations is obtained by integrating the definite integrals

$$p_1 = \frac{9}{20}\left[\frac{(\alpha-\beta)}{2}\left\{\frac{40\varepsilon^2-3}{f^4}+\frac{20f^2\varepsilon^2-3(\varepsilon-1)^2}{(\varepsilon-1)^6}\right\}-\frac{3\,\mathrm{Re}}{7}\left\{\frac{1}{f^2}+\frac{1}{(\varepsilon-1)^2}\right\}\right] \tag{45}$$

which involves the relaxation and retardation time parameters. It is observed that the first order pressure for viscous case could be found by setting $\alpha = \beta = 0$. One can obtain first order pressure for Maxwell and Jeffrey fluid by setting $\beta = 0$ and $\alpha = 0$ respectively.

4.4.3. Second order pressure and solution

Comparing the coefficients of δ^2, we arrive at

$$\frac{\partial p_2}{\partial x} + \mathrm{Re}\left(\frac{\partial \psi_o}{\partial y}\frac{\partial^2 \psi_1}{\partial x \partial y} + \frac{\partial \psi_1}{\partial y}\frac{\partial^2 \psi_o}{\partial x \partial y} - \frac{\partial \psi_o}{\partial x}\frac{\partial^2 \psi_1}{\partial y^2} - \frac{\partial \psi_1}{\partial x}\frac{\partial^2 \psi_o}{\partial y^2}\right) = \frac{\partial S_{xx}^{(1)}}{\partial x} + \frac{\partial S_{yx}^{(2)}}{\partial y} \tag{46}$$

$$\frac{\partial p_2}{\partial y} = \frac{\partial S_{yx}^{(o)}}{\partial x} + \frac{\partial S_{yy}^{(1)}}{\partial y} \tag{47}$$

Integral form of solution of above two equations is obtained by similar method used for first order pressure as

$$\begin{aligned} p_2 = {} & \frac{9\eta f'}{280 f^6}\{\,84\eta\{\,\alpha\beta\left(20\eta^2-7\right)-2\beta^2\left(5\eta^2-3\right)-\alpha^2\left(10\eta^2-1\right)\,\}+(\alpha-\beta)f^2\{\,140\left(3\eta^2-1\right) \\ & -\mathrm{Re}\,\eta\left(21\eta^4-70\eta^2+33\right)\,\}+70\eta f^4\,\}+\frac{3}{107800}\int_0^x\{\,\frac{f'^2}{f^7}\{\,5544\{\,\alpha\beta\left(-3500\eta^4+980\eta^2+107\right) \\ & +2\beta^2\left(875\eta^4-420\eta^2+12\right)+\alpha^2\left(1750\eta^4-140\eta^2-131\right)\,\}-231(\alpha-\beta)f^2\{\,175\alpha\left(84\eta^3-20\eta-3\right) \\ & -2\,\mathrm{Re}\left(525\eta^6-1400\eta^4+495\eta^2+8\right)-4f^4\left(52\,\mathrm{Re}^2+2695\left(3\eta^2-7\right)\right)\,\}+\frac{f''}{f^6}\{\,2772\{\,\alpha\beta(\,700\eta^4 \\ & -245\eta^2-18\,)-2\beta^2\left(175\eta^4-105\eta^2+3\right)-\alpha^2\left(350\eta^4-35\eta^2-24\right)\,\}+231(\alpha-\beta)f^2\{\,700\alpha\eta \\ & \left(3\eta^2-1\right)-\mathrm{Re}\left(105\eta^6-350\eta^4+165\eta^2+8\right)+2f^4\left(78\,\mathrm{Re}^2+2695\left(15\eta^2-1\right)\right)\,\}\,\}dx \end{aligned} \tag{48}$$

Second order pressure is more general and one can obtain second order pressure for Newtonian fluids by setting $\alpha = \beta = 0$. Second order pressure for Maxwell fluid is easily obtained by setting $\beta = 0$. Second order pressure for Jeffrey fluid could be obtained by setting $\alpha = 0$.

5. VELOCITY FIELD AND WALL SHEAR STRESS

The velocity components u and v could be find easily by making use of ψ from (22) in (12).

Wall shear stress is defined as

$$\tau_{\omega} = S_{yx} \tag{49}$$

and up to second order is given by

$$S_{yx} = S_{yx}^{(o)} + \delta S_{yx}^{(1)} + \delta^2 S_{yx}^{(2)} \tag{50}$$

or

$$\tau_{\omega} = \frac{3}{2f^2} + \frac{\delta}{f^4}\left(\frac{3\,\mathrm{Re}\,f'f^2}{35} - \frac{63}{10}(\alpha-\beta)f'\right) + \frac{\delta^2}{f^6}\left\{\frac{423f'^2}{175}\left(11\alpha^2 - 17\alpha\beta + 6\beta^2\right) - \frac{f'^2 f^4}{10}\left(39 + \frac{79\,\mathrm{Re}^2}{2895}\right)\right.$$
$$\left. + \frac{9\alpha(\alpha-\beta)}{8f^3} - \frac{9(\alpha-\beta)f'^2 f^2}{350}(22\,\mathrm{Re} + 350\alpha) - \frac{9ff''}{350}\left(103\alpha^2 - 121\alpha\beta + 18\beta^2\right) + \frac{f''f^5}{2695}\left(1617 + 4\,\mathrm{Re}^2\right)\right\} \tag{51}$$

The points of separation and reattachment are given by $\tau_{\omega} = 0$, the resulting equation is quadratic in Re and the solution in terms of Re is

$$\mathrm{Re} = \frac{-b \pm \sqrt{b^2 - 4ac}}{2a} \tag{52}$$

where

$$a = 4\delta^2 f^4\left(40ff'' - 79f'^2\right) \tag{53}$$

$$b = 9240\delta f^2 f'\left(f^2 - \frac{33\delta f'}{5}(\alpha-\beta)\right) \tag{54}$$

$$c = 231\left\{1128\delta^2 f'^2\left(11\alpha^2 - 17\alpha\beta + \beta^2\right) - 420\delta f^2 f'(\alpha-\beta)(7 + 10\delta\alpha f') - 140f^4\left(13\delta^2 f'^2 - 5\right)\right.$$
$$\left. - 12\delta^2 ff''\left(103\alpha^2 - 121\alpha\beta + 18\beta^2\right) + 525\alpha\delta^2 f^3 f''(\alpha-\beta) + 280\delta^2 f^5 f''\right\} \tag{55}$$

Equation (52) gives the separation and reattachment points.

6. GRAPHICAL DISCUSSION

In this section solutions are presented graphically for stream lines, wall shear stress, zero wall shear stress, pressure gradient and velocity profile by using different values of parameters. Solutions are analyzed numerically for the relaxation time (α), retardation time (β), height of constriction (ε) and Reynolds number (Re).

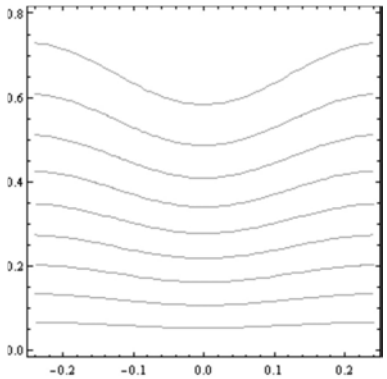

Figure 2(a)

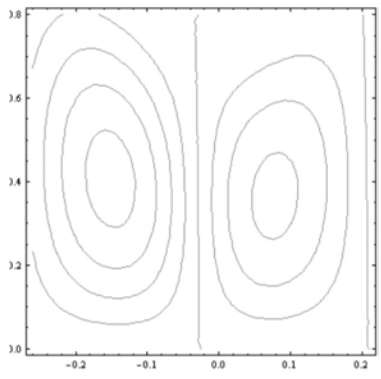

Figure 2(b)

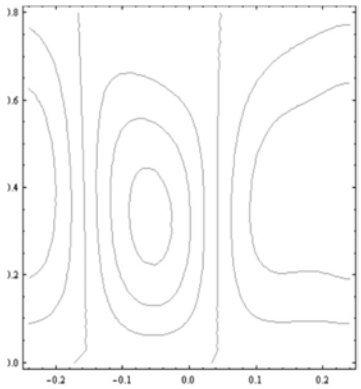

Figure 2(c)

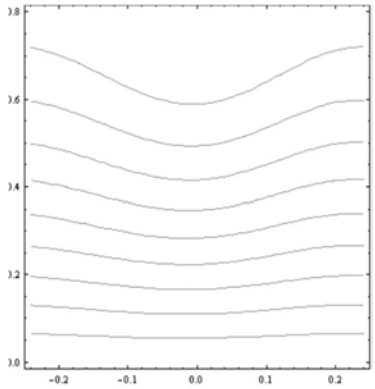

Figure 2(d)

Figure 2 presents the behavior of stream lines for zeroth order 2(a), first order 2(b), second order 2(c) and up to second order 2(d) respectively for $\mathrm{Re} = 12,\ \varepsilon = 0.2,\ \delta = 0.1,\ \alpha = 0.04,\ \beta = 0.2.$. In these figures $x - axis$ is taken in the horizontal direction and $y - axis$ perpendicular to it. The zeroth order solution corresponds to laminar flow and similar to Newtonian fluid, first order solution induces the clockwise and counterclockwise rotational motion in the converging and diverging regions, which indicates the separation point in the converging region and reattachment point in the diverging region. Figure 2(c) shows the stream lines for second order solution which mentions the rotational motion and indicates the separation and reattachment region. Figure 2(d) presents the stream line solution up to second order. By setting $\alpha = 0,\ \beta = 0$, stream lines are similar to [6].

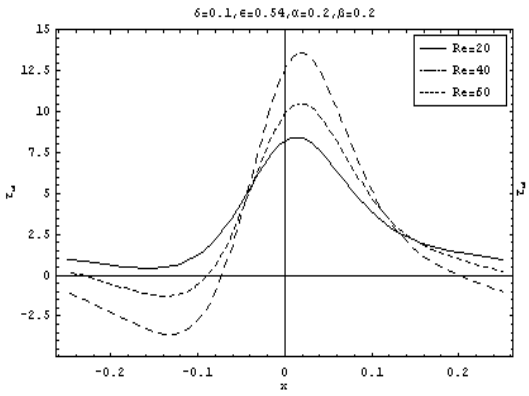

Figure 3: Effect of Re on wall shear stress.

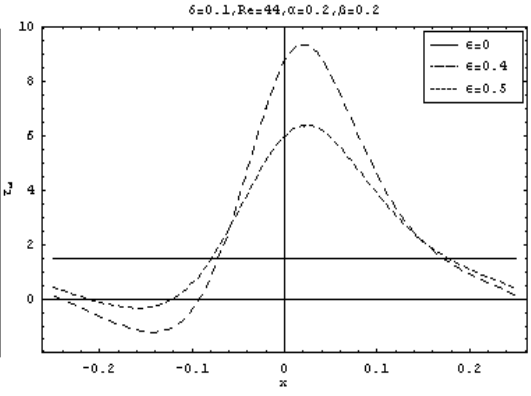

Figure 4: Effect of ε on wall shear stress.

Figure 3 depicts the distribution of wall shear stress for Re by using the fixed values of $\varepsilon = 0.54,\ \delta = 0.1,\ \alpha = 0.2,\ \beta = 0.2.$ It is observed that by the increase in Re, the negative shearing increases in the converging and diverging section of the channel and becomes high near the throat of stenosed region. The negative shearing in the converging and diverging section of the channel indicates that there is point of separation in the upstream region and reattachment in the downstream region of the channel.

In figure 4 effect of height of stenosis (ε) is presented for wall shear stress. The straight line indicates that there is no stenosis and the flow is known as Poiseuille

flow. It is observed that by the increase in ε wall shear stress decreases and becomes negative in the converging section of the channel, which is the prediction of separation point. The separation point is the point nearest the throat where the reversed flow along the wall of the channel could be observed. The point farthest down the stream from the throat where back flow occurs is defined as the reattachment point.

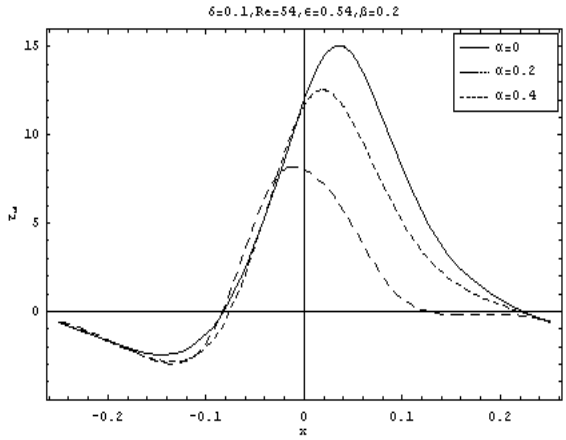

Figure 5: Effect of α on wall shear stress.

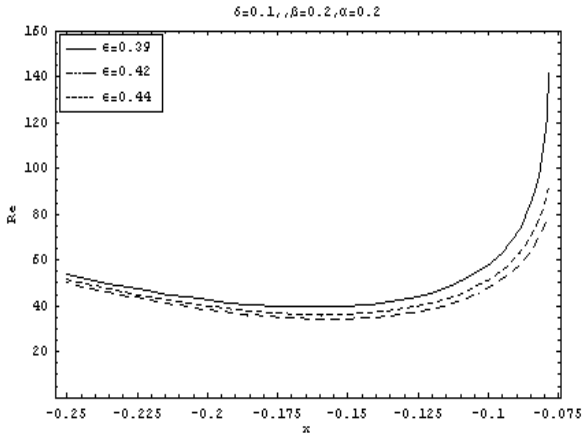

Figure 6: Separation point for ε in converging region.

Figure 5 mention the effect of relaxation time (α) on wall shear stress in converging and diverging sections of the channel by using the fixed values of $\mathrm{Re}, \varepsilon, \delta, \beta$. We note that for $\alpha = 0, \beta = 0$ the effect of wall shear stress is similar as the viscous fluid. We also observed that the wall shear stress decreases near the throat of the channel by increasing α.

Figure 6 predicts the separation point for the different values of height of stenosis (ε) in the converging region using fixed values of δ, α and β. It is observed that the critical Reynolds number decreases by increasing ε. The aim of analysis is to obtain the critical Reynolds number where the separation point occurs.

Figure 7 presents zero wall shear stress for the variation of retardation time (β) along with the constant values of δ, α and ε in the converging region of the channel. The purpose of investigation is to determine the critical value of β at which separation occurred in the converging region of the channel. It is found that as the value of β increases the critical value of Re increases.

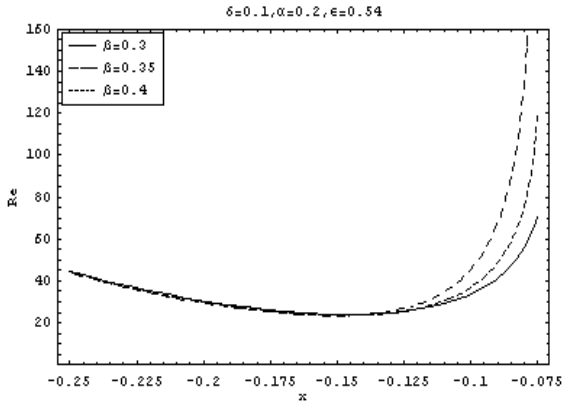

Figure 7: Separation point for β in converging region.

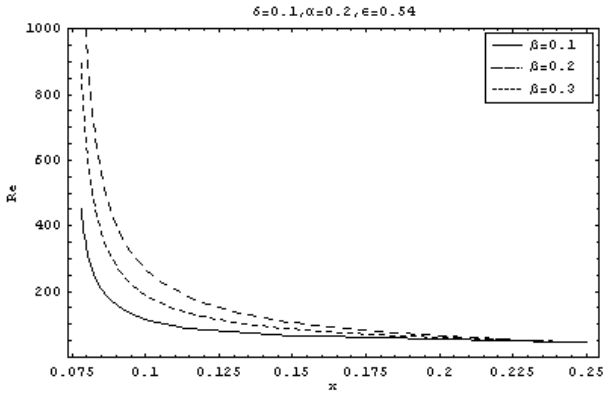

Figure 8: Reattachment point for β in the diverging region.

Figure 8 shows the effects of zero wall shear stress for different values of retardation time (β) together with fixed values of ε and α. Our aim is to investigate about the critical value of Re at which reattachment occurred in the diverging region of the channel. It is observed that as the critical Reynolds number Re reached the reattachment occurs in the diverging region of the channel. It is also found that the critical value of Re increases as β increases in the diverging region of the channel.

Figure 9 predicts the effect of height of stenosis (ε) on axial component of velocity by using the fixed values of Re, α and β. The straight line indicates that there is zero height of stenosis and the flow in this case is Poiseuille flow. It is noted that as ε increases the velocity increases over the stenosis and becomes negative in the converging and diverging region of the channel. The negative velocity indicates the

reverse flow which predicts the separation and reattachment points. Figure 10 presents the effect of relaxation time (α) over the axial velocity of the blood. It is observed that by the increase in α axial velocity becomes negative in the converging as well as diverging section of the channel and decreases over the stenosis. Negative velocity predicts the back flow in the converging and diverging region of the channel. The separation point in the converging region and reattachment point in the diverging region of the channel are due to back flow.

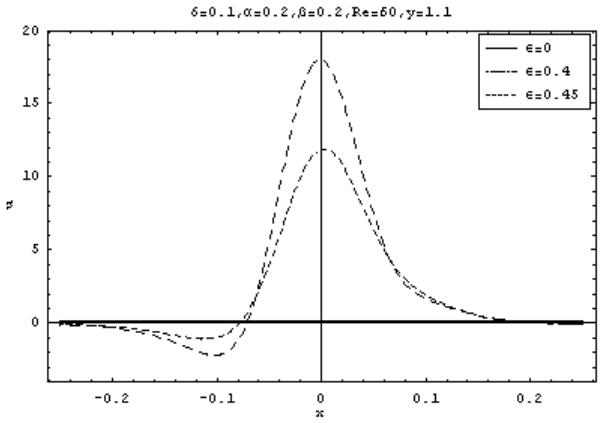

Figure 9: Velocity distribution for ε .

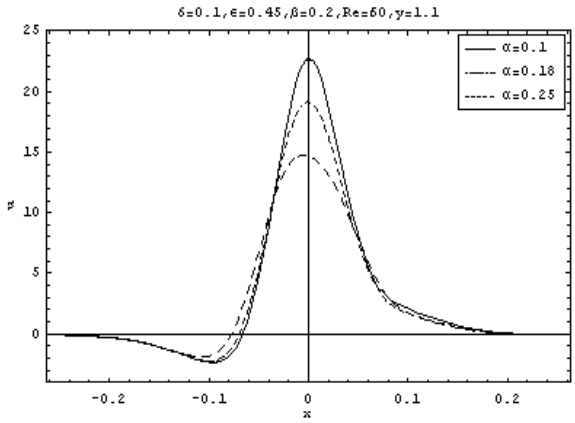

Figure 10: Velocity distribution for α .

Figure 11 depicts the distribution of pressure gradient for relaxation time (α) about the line $y = 1.1.$ It is found that by the increase in α the pressure gradient decreases over the stenosed region and obtain parabolic shape. It is noted that due to reverse flow the pressure gradient becomes negative in the converging as well as in the diverging section of the channel. Figure 12 shows the distribution of pressure gradient about the line $y = 1.1$ for retardation time (β) with fixed values of other parameters. It is observed that by the increase in β pressure gradient increases over the stenosed region and obtains parabolic shape. It is noted that due to reverse

flow pressure gradient becomes negative in the converging as well as in the diverging regions of the channel.

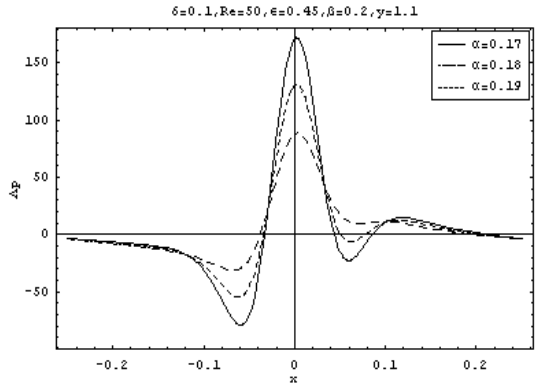

Figure 11: Pressure gradient for α .

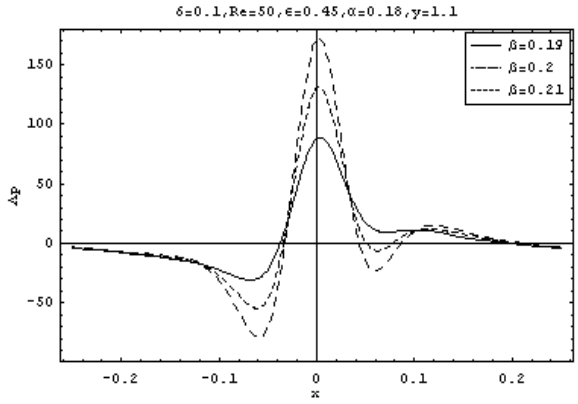

Figure 12: Pressure gradient for β .

7. DEDUCTIONS

The current investigations for Oldroyd-B fluid is more general and can be deduced to the following results:

(i) Newtonian fluids by setting λ_1 , λ_2 equal to zero.

(ii) Maxwell fluid by setting λ_2 equal to zero.

(iii) Jeffrey fluid by setting λ_1 equal to zero.

(iv) Second grade fluid by substituting $\lambda_1 = 0$, $\mu\lambda_2 = \alpha_1$.

8. CONCLUSIONS

In the current analysis the basic governing equations of fluid flow are modeled for the Oldroyd-B fluid. The resulting equations are transformed into stream function formulation and find the compatibility equation in terms of ψ . The Oldroyd-B fluid is analyzed analytically for velocity component, pressure gradient, wall shear stress, separation and reattachment points by using the regular perturbation method with

δ as a small parameter. From the graphical representation it is observed that the solution obtained in this analysis are more general. The general patron of streamlines is same as in [4, 5] by setting λ_1, λ_2 equal to zero. The wall shear stress is similar as [2, 3] and separation and reattachment points are similar with [3]. It is observed the following:

(i) Wall shear stress and pressure gradient increases with the increase in Re.

(ii) By the increase in ε increases the wall shear stress and pressure gradient.

(iii) Critical Re decreases by the increase in ε.

(iv) Increase in α increases in pressure gradient, velocity and wall shear stress.

(v) Critical Re decreases by the increase in α in the converging and diverging region.

REFERENCES

1. D. F. Young, Effect of a time-dependent stenosis on flow through a tube., J. Engg Ind., Trans. Am. Soc. Mech. Engrs., 90(1968) 248-254.
2. J. H. Forrester and D.F. Young, Flow through a converging-diverging tube and its implications in occlusive vascular disease. J. Biomech., 3 (1970) 297-316.
3. J. S. Lee and Y.C. Fung, Flow in locally constricted tubes at low Reynolds number. J. Appl. Mech., 37(1970) 9-16.
4. B. E. Morgan and D.F. Young, An integral method for the analysis of flow in arterial stenosis, J. Math. Biol. 36 (1974) 39-53.
5. K. Haldar, Analysis of separation of blood flow in constricted arteries, Archives of Mechanics, 43 (1) (1991) 107-113.
6. Joseph C. F. Chow and Kunihisa Soda, Laminar flow in tubes with constriction, The Physics of Fluids, 15 (10) (1972) 1700-1706.
7. J. B. Shukla, R. S. Parihar and B. R. P. Rao, Effects of stenosis on Non-Newtonian flow of the blood in an artery, Bull. of Math. Bio., 42 (1980) 283-294.
8. J. C. Mishra and G. C. Shit, Blood flow through arteries in a pathological state, a theoretical study, Int. J. of Eng. Sci., 44 (2006) 662-671.
9. K. Haldar, Effect of the shape of stenosis on the resistance to blood flow through an artery, Bull. of Math. Bio., 47 (4) (1985) 545-550.
10. Cheng Tu and Michel Deville, Pulsatile flow of non- Newtonian fluids through arterial stenoses, J. Biomech., 29 (7) (1996) 899-908.
11. Azhar Mirza, Ali R Ansari, Abdul M Siddiqui and Tahira Haroon, On the steady two-dimensional flow of blood with heat transfer in the presence of a stenosis, WSEAS Transactions on Fluid Mechanics, 8 (4) (2013) 149-158.
12. A. A. Mirza, A. M. Siddiqui and T. Haroon, Atherosclerotic Study of non-Isothermal non-Newtonian Steady Flow of Blood in a Plane by Adomian

Decomposition Method, International Research Journal of Biological Sciences, 5 (4) (2016) 54-63.

PK ISSN 0022- 2941; CODEN JNSMAC
Vol. 56, (2016) PP 32-47

MECHANICAL BEHAVIOR OF LASER IRRADIATED Al-Cu ALLOY CORRELATED WITH SURFACE AND STRUCTURAL MODIFICATIONS

DANIEL YOUSAF[1], SHAZIA BASHIR[1], SHAHBAZ AHMAD[1,2], UMM-I-KALSOOM[1] AND MAHREEN AKRAM[1]

1. Center for advanced Studies in Physics, G. C. University, Lahore, Pakistan
2. Department of Physics, University of Sargodha, Lahore Campus

danielfccollege@gmail.com

ABSTRACT

The correlation of mechanical behavior with surface and structural modifications of laser irradiated Al-Cu alloy 2024 for various laser pulses has been investigated. The specimens were exposed to Excimer (KrF) laser (248 nm, 18 nsec) with a fluence of 4.3 J/cm^2 for different laser pulses ranging from 750 to 3750 under vacuum condition. The surface and structural modifications of laser irradiated specimens were investigated by Scanning Electron Microscope (SEM) and X-ray Diffractometer (XRD) respectively. SEM analysis reveals the formation of micro-sized craters along with the growth of the periodic surface structures (ripples) at their peripheries attributed to thermal ablation and energy deposition. The size of the craters initially increases and then decreases due to energy deposition by increasing the number of pulses. XRD analysis shows an anomalous trend in the peak intensity, crystallite size and dislocation density of irradiated specimen for various number of laser pulses. This variation in the peak intensity and crystal size is due to non-uniform thermal stresses, recrystallization and incubation effect. In order to investigate the mechanical properties of the irradiated specimens, Universal Tensile Testing machine and Vicker Microhardness tester were employed. The changes in Ultimate Tensile Strength (UTS), Yield Strength (YS) and microhardness were found to be anomalous for various number of laser pulses. These changes in mechanical properties can be attributed to variation in the defect density and residual stresses. The change in the surface and structural properties of Al- Cu alloy 2024 after laser irradiation has been associated with the modification in its mechanical properties.

Keywords: Laser fluence, Structural modification, Microhardness, Mechanical properties, Surface morphology

1. INTRODUCTION

The interaction of high-power laser pulses with solids has been studied since the early stages of laser development [1]. The pulsed laser irradiation (PLI) is a technique employed in the past years for different applications, such as pulsed plasma production, thin film deposition, production of ions at high charge states or ion emission and ablation of high boiling point materials [2]. At high laser energy, the material evaporated from the target surface is strongly ionized and instantaneously hot plasma is produced, which expands very fast in vacuum. The plasma becomes an intense source of electrons, ions, neutrals and energetic photons [3]. There is a great deal of interest in utilizing laser ablation and crater formation for practical applications. However, the ablation mechanism and craters formation both strongly depend on laser pulse parameters and the material properties. In the literature, many researchers reported about the properties of the plasma generated by pulsed laser irradiation [4].

Al-Cu alloy 2024 is an important engineering material which has high strength to weight ratio, good fatigue resistance, high thermal and electrical conductivity. It is widely used in aircraft, especially for wings and fuselage structures. Due to its widespread use in automotive and aerospace industry, it is of fundamental importance and interest to explore the surface, structural and mechanical properties of Al-Cu alloy 2024 after laser irradiation [5]. In this regard, Cheng et al [6] investigated the effects of laser pulses and number of scans on the micro-processing quality and efficiency of Al-Cu alloy 2024. It was found that ablation rate of alloy changed dramatically with number of laser pulses due to the combined effects of plasma, residual thermal energy and phase transition. Dou et al [7] studied surface texturing effects of Al-Cu alloy 2024 using femtosecond and nanosecond pulse laser irradiation and found that surface features ranging from nano to micro-dimensions can be developed through variation in laser energy. They also observed that ultraviolet (UV) laser pulses provide a mechanism for the alteration of surface morphology and texturing without significant damage of the underlying material. Clauer et al [8]. reported an increase in hardness, stress, ultimate tensile stress and decrease in ductility of Aluminum alloy after high intensity laser induced stress waves interaction.

In our previously reported work [9], similar results have been found by irradiating Al-Cu alloy 2024 at various fluences ranging from 3.8 J/cm^2 to 5.5 J/cm^2 with fixed laser pulses. By increasing the fluence, energy deposition increases due to which changes in surface, structural and mechanical properties have been observed.

According to our knowledge very little work is reported in which surface, structural and mechanical properties of Al-Cu alloy after laser irradiation are investigated. The purpose of the present work is to investigate the effect of various number of laser pulses on the surface, structural and mechanical properties of Al-Cu alloy under

vacuum condition. SEM analysis was carried out to explore surface modifications. These surface morphological changes were correlated with structural modification of Al-Cu alloy explored by XRD analysis. In order to establish the correlation of these surface and compositional changes with mechanical properties of the material, the tensile testing and Vickers micro hardness testing techniques were employed which is the novelty of this work.

2. EXPERIMENTAL WORK

The Al-Cu alloy 2024 with composition of aluminum 93.5 %, copper 4.3-4.5%, magnesium 1.3-1.5% and manganese 0.5-0.6% was used for this experiment. Samples in the form of rectangular bar shape of Al-Cu alloy with thickness of 3 mm, length of 45 mm and width of 6 mm were selected for irradiation. The surface of the samples was polished with silicon carbide (SiC) papers of different grades (grit size 400-2000) and then mechanically polished with diamond paste (6-1 μm). The polished samples were annealed under vacuum condition of 10^{-6} Torr by incorporating them in pyrex glass tubes at a temperature of 300 ^{0}C in a muffle furnace for 120 minutes. After mounting the samples on the sample holder attached with D.C motor, they were placed in the chamber, which was evacuated to the base pressure of 10^{-3} Torr. Excimer laser (KrF) of wavelength 248 nm, pulse duration of 18 ns, pulse energy of 100 mJ at a fluence of 4.3 J/cm^2 was employed to irradiate the samples under vacuum condition. After passing through a plano-convex lens of focal length 50 cm, laser beam was focused with spot area of 0.0235 cm^2 perpendicular to the target surface placed in the chamber. The whole experiment was performed at room temperature. In order to irradiate the whole surface area 45x1 mm^2 of alloy sample, laser beam was fixed during irradiation and the samples were scanned uniformly with the help of a D.C motor with the scanning speed of 0.6 mm sec^{-1}. The targets were exposed for five various numbers of laser pulses of 750, 1500, 2250, 3000, 3750 respectively. The surface morphology of irradiated targets was investigated by Scanning Electron Microscope (SEM) (JEOL-JSM-6480LV). In order to determine the crystallographic structure and phase analysis of exposed targets, X-ray diffractometer (XRD) (X'Pert PRO (MPD) was employed. The unirradiated and irradiated samples were then deformed using a Vickers hardness tester (Zwick / Roell ZHU5030) and a Universal Tensile testing Machine (UTM) (AG-1 Shimadzu) to investigate microhardness and mechanical properties of Al-Cu alloy 2024.

3. RESULT AND DISCUSSIONS

3.1. Surface morphology

SEM images of (a) un-irradiated and irradiated Al-Cu alloy 2024 with laser at fluence of 4.3 J/cm^2 with repetition rate of 30 Hz for various number of laser pulses of (b) 750 (c) 1500 (d) 2250 (e) 3000 and (f) 3750 are shown in figure 1. The figure shows that

after 750 pulses irradiation, a few micro-sized craters, ridges and well defined periodic surface structure called ripples around the periphery of craters are observed in Fig.1 (b). When the laser pulses are increased to 1500, the size of craters increases but the density of the laser-induced craters decreases as revealed in figure 1 (c). The appearance of multiple ablative layers or ripples becomes distinct and wider at this laser pulses. By increasing laser pulses up to 2250, the size and density of the craters increases as shown in figure 1 (d). The appearance of multiple ablative layers or ripples around the periphery of the craters merges at this number of laser pulses. Merging of multiple ablative layers at this particular number of pulses is due to high degree of heating and melting. The edges of these craters are found to be uplifted. As the number of laser pulses are further increased to 3000, the size of the craters decreases significantly and its density increases as is exhibited in figure 1 (e). Multiple ablative layers or ripples become more prominent for these laser pulses. Figure 1 (f) depicts that at maximum laser pulses of 3750, the size of craters again increases significantly and their appearance becomes more distinct where as no change in the density is observed. The crater formation observed in figure 1(b-d) is attributed to thermal ablation on the basis of laser induced heating, thermal desorption, melting and explosive boiling of the target surface [10]. The laser energy density on the target for nanosecond pulses is of values of several 10^6 J/cm^2. Focusing a beam of a high-power nanosecond pulse laser onto a solid target causes transferring considerable part of the beam energy and momentum to the target. The rapid heating of surface material yields a high pressure of the order of mega bars. As a result, a shock wave is generated with typical velocity up to several km/s. In these conditions, a violent evaporation of the target material follows and in the place where laser radiation is impinging, a crater is formed. The dimension of the crater depends on the laser beam parameters (the laser intensity, the focused spot size, the laser pulse duration) as well as on the physical properties of the target material. A shock wave passing completely through the target is followed by a rarefaction wave moving into the compressed material behind the original shock wave [11]. Pulse laser ablations in nanoseconds regimes is considered as a superposition of heating, melting, vaporization and melt ejection under the action of the plasma recoil pressure. When the pressure of the plasma/vapor exceeds the surrounding pressure, the molten material can be expelled explosively from the surface of the sample due to the violent recoil pressure [12]. As a consequent, the crater is formed. The increase in recoil pressure due to large energy deposition by increasing number of laser pulses causes enhancement in the size of craters. Laser material interaction causes the development of compressive stresses. These stresses are responsible for the formation of defects in the interior of craters. The variations in the size distribution of craters can be attributed to the large number of surface defects such as contaminants, small pits, oxides and other heterogeneities. These defects generally show a higher sensitivity to laser absorption than the bulk material and hence causes

the non-uniform laser energy absorption inside the material [13]. The formation of the ripples (periodicity) in the periphery of the craters can be attributed to the excitation of the surface plasmons to induce the periodic enhancement of local fields in the surface layer. The interaction between the incident laser light and the excited surface plasmons created at the irradiated material interface causes periodical thermal gradient and variations in periodic intensity on the surface of the material. The melted material moves from the hot regions to colder region (Marangoni effect) and consequently periodic structures are formed by a self-organized process [14].

The initial increasing trend of crater size with increasing laser pulses up to 1500 is due to the more energy deposition which means that the energy received by the material per unit area increases and correspondingly large scale material deformation and imprinting occurs [15].

The mechanism of the crater formation and change in its size can also be interpreted in terms of heat diffusion into the irradiated target. When the irradiation energy is higher than the ablation threshold, it leads to an ionization and results in a plasma formation. The plasma formation and expansion is associated with the occurrence of the material ejection [16]. Fusion and evaporation takes place if the surface temperature exceeds the melting and evaporation temperature of that material. The phenomena of melting and vaporization can be observed from the presence of molten materials around the craters [17]. By increasing laser pulses from 2250 to 3000, the crater size decreases and crater density increases. This reduction in crater size is attributed to refilling of cavities and due to the resolidification process in the melted material.

The size of the craters increases at the maximum laser pulses of 3750 due to intense melting and ablation of the material as is displayed in Figure 1 (f) [18]. We conclude that energy deposition, recoil violent pressure and the surface defects are responsible for the production and variation of craters size and craters density. Hence, considering melting, resolidification processes with the variation in the sizes of craters, we can conclude that by increasing number of laser pulses, the size of craters increases but after certain number of laser pulses, reduction in the size of craters is observed due to refilling and resolidification process.

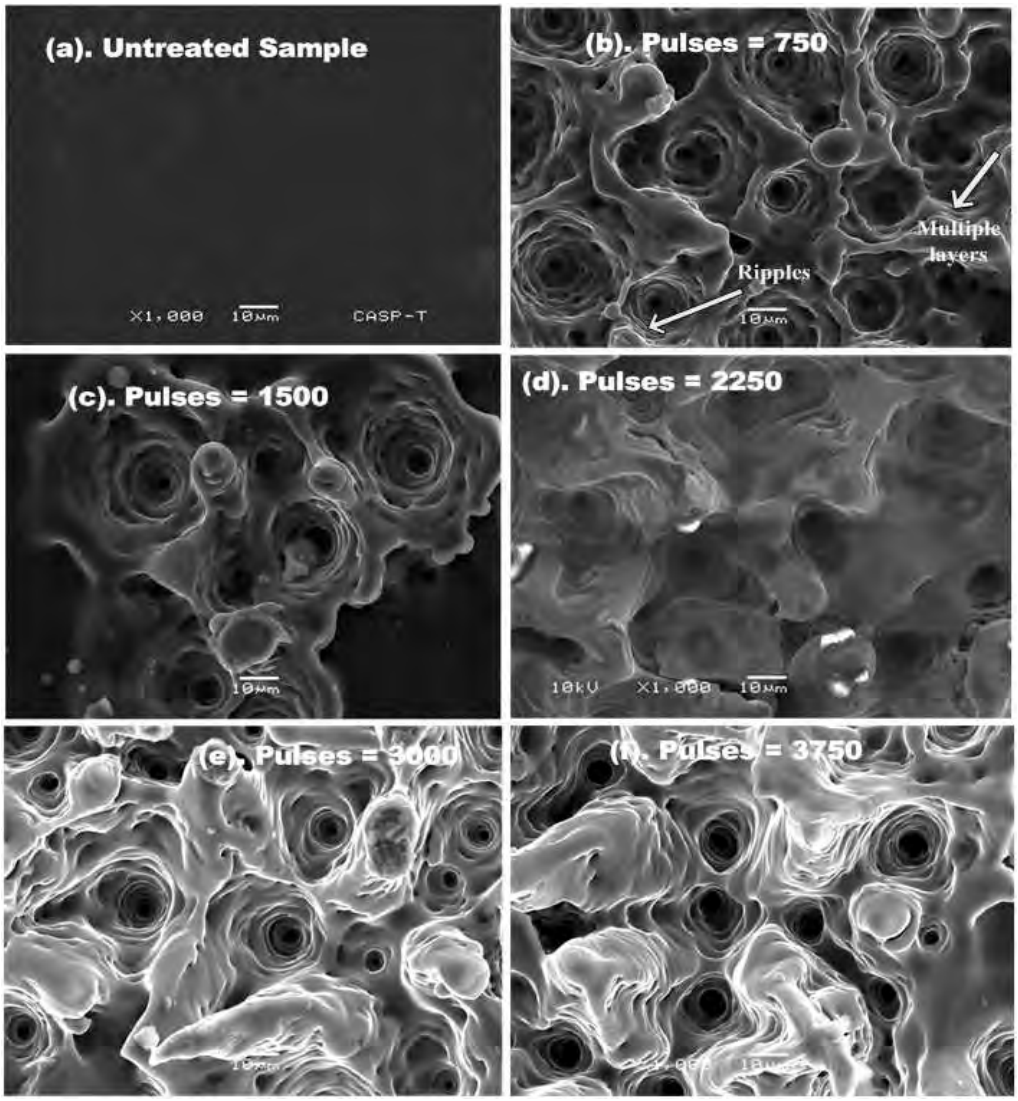

Figure 1: SEM micrographs revealing the comparison of variation in surface morphology of

(a) unirradiated and Excimer-laser irradiated Al-Cu alloy 2024 for a fluence of 4.3 J/cm^2 at wavelength of 248 nm, pulse duration of 18 ns for various number of laser pulses of (b) 750 (c) 1500 (d) 2250 (e) 3000 and (f) 3750.

3.2. XRD analysis

XRD technique is used to obtain phase identification, variation in crystallinity and dislocation densities of the irradiated material. Figure 2 depicts the XRD patterns of (a) un-irradiated and laser irradiated Al-Cu alloy 2024 under the vacuum condition for various number of laser pulses of (b) 750 (c) 1500 (d) 2250 (e) 3000 and (f) 3750. The diffraction peaks corresponding to (222), (213), (440), (622) planes for un-irradiated sample are identified at angles 38^0, 45^0, 65^0, 78^0. Whereas for irradiated samples, peaks corresponds to planes (131), (213), (062), (622) at angles 39^0, 46^0, 66^0 and 79^0 with small peak shifting are observed. Peak shifting indicates generation

of compressive and residual stresses on the surface of the Al-Cu alloy. The residual stresses are developed on the target surface after laser irradiation and the effect of these stresses plays a significant role for the strengthening of metals. These stresses result from differential expansion (or contraction) of lattice on the exposed target surface related to thermal expansion mismatch, phase transformations, differential diffusion of different elements, or defects generation during irradiation [19]. Peak shifting towards the higher angular position indicates compressive stresses whereas shifting towards lower angular position indicates tensile stresses [20]. From figure 2, phase changes from Al_2MgO_4 to Al_2CuMg and Al_2CuO_4 are observed at angles of 39^0 and 66^0. These new phases are formed due to the rapid heating and quenching effect induced by laser irradiation. During rapid heating and cooling, residual and thermal stresses are generated in the surface of the material due to tremendous change in temperature. These stresses are associated with the change in volume and phase transformation. The melting, resolidification and redeposition processes as a result of laser irradiation are also responsible for the formation of new phases [21]. Both the peak intensity and crystallographic alteration of alloy shows an anomalous behavior for various number of laser pulses. The variations in the peak intensity and shifting are attributed to scattering effects, non uniform thermal stresses, recrystallization and non-uniform conduction of the energy absorbed by the atoms as the result of laser irradiation [22]. The variation in the average peak intensity is related to the variation in the crystallite size and strain induced on the sample surface after laser irradiation. Many other research groups have also investigated the effect of increasing number of laser pulses on the metals and metallic alloys to study the structural modification [23].

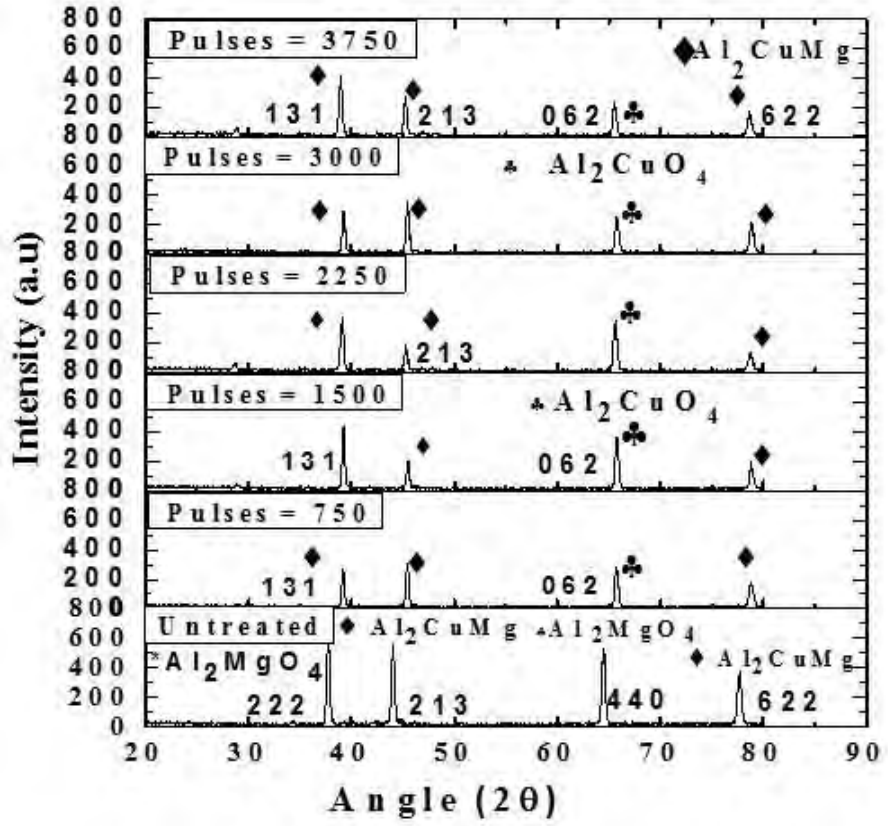

Figure 2: XRD pattern of (a) unirradiated and laser- irradiated Al-Cu alloy 2024 for a fluence of 4.3 J/cm^2 for various number of laser pulses.

When the number of pulses is increased, the deposited energy on the target surface also increases due to accumulation effects. Initial pulses will produce incubation effect which causes changes in optical, mechanical and chemical properties of the material. Production of defects, impurities, voids and inhomogenities in the material is due to this incubation effect. This will also enhance optical absorption of forthcoming pulses. Here, we are also trying to investigate the structural changes for various number of laser pulses of laser beam with constant fluence of value 4.3 J/cm^2. The deposited energy is therefore, not constant for various number of laser pulses. The enhanced energy deposition may cause the enhancement in defect generation and dislocation densities. These effects may also induce the variation in stresses (compressive, tensile) and crystallite size as can be seen from the figure 3 & 4.

Initially, the peak intensity of plane (062) decreases at the laser pulses of 750 as compared to untreated samples. By increasing the laser pulses up to 1500 to 2250, both the peak intensity and crystal size increase. This increase in peak intensity and crystal size are attributed to the enhancement of diffraction of X-ray from target and the crystal growth caused by atomic diffusion of most atoms across the grain boundaries after laser material interaction [24].

Further increase in laser pulses from 2250 to 3000 causes reduction in peak intensity and crystal size. This reduction in peak intensity is due to the re-crystallization phenomenon during resolidification after melting. Large sized grains break up into the smaller ones after laser irradiation and cause the attenuation in the peak intensity. With the further increase of laser pulses up to a maximum value of 3750 causes enhancement of peak intensity which is related to the enhanced crystal growth due to maximum energy deposition. Thus, by increasing the laser pulses, the energy deposition increases which enhances the generation of defects. The defects are then annealed. Hence, the peak intensities initially increase then decrease and finally increase showing anomalous behavior.

The crystallite size was evaluated using Scherer's formula [25].

$$\text{Crystallite Size } (D) = 0.9\,\lambda / \beta\cos\theta \qquad (1)$$

Where "λ" is wavelength of X-rays in (nm), "β" is full width half maxima and "θ" is the angle of X-rays diffractometer. The variation of average crystallite size with various number of laser pulses is shown in figure 3. The crystallite size initially increases then decreases and finally increases.

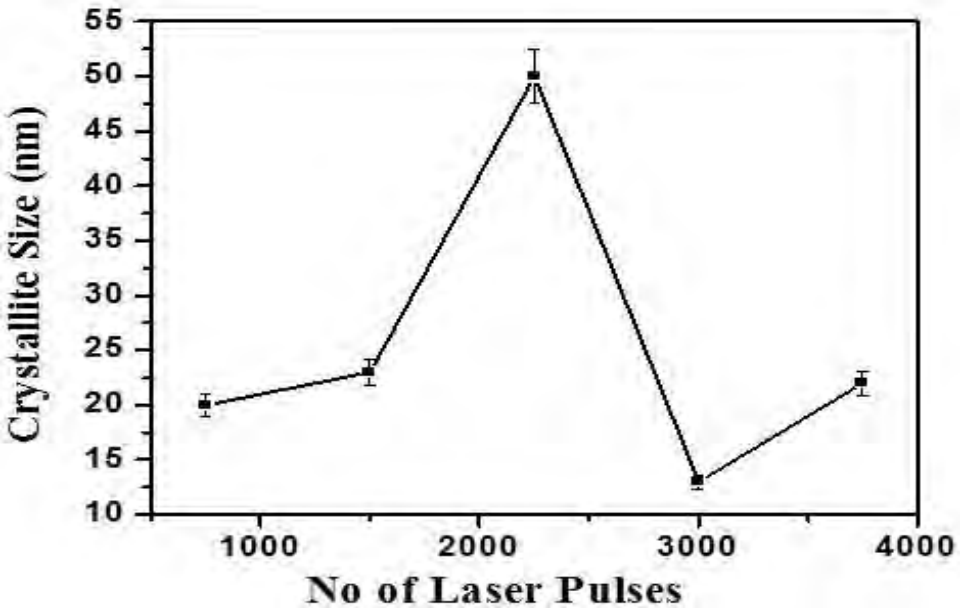

Figure 3: The variation in the crystallite size of laser irradiated Al-Cu alloy 2024 for various number of laser pulses.

The dislocation density is evaluated by using following formula [26].

$$\text{Dislocation Density} = 1/(\text{Crystallite Size})^2 \qquad (2)$$

The dislocation density initially decreases, then increases and ultimately decreases as revealed in figure. 4. Compressive residual stresses are produced on the target material after laser irradiation due to defect generation, thermal expansion or phase transformation. Compressive waves and high pressure (GPa) due to volumetric absorption of energy can also produce compressive waves. By increasing number of pulses, compressive stresses increase and hence causes decrease of crystallite size and vice verse [27]. By increasing number of laser pulses, compressive residual

stresses get relaxed and hence causes for the enhancement of crystallite size. Whereas, the dislocation density initially decreases, then increases and ultimately decreases. Hence, both crystallite size and dislocation density shows anomalous behavior. This variation in the crystallite size and dislocation density is also attributed to the thermal stresses, lattice defects and recovery processes [28].

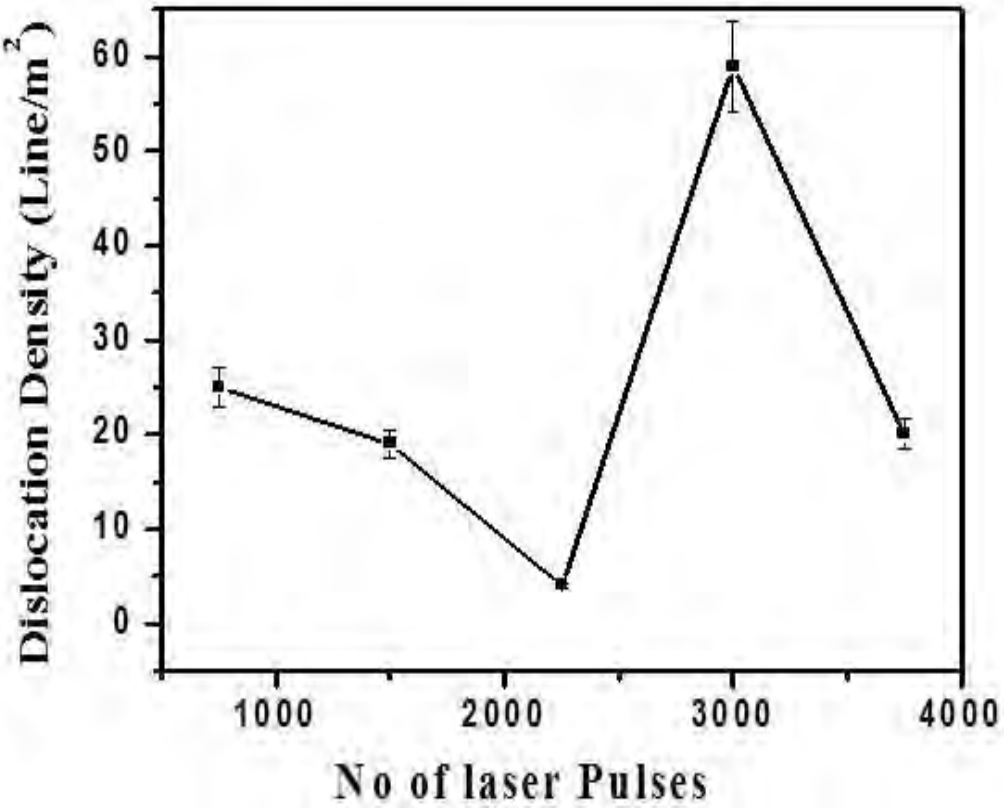

Figure 4: The variation of dislocation density of Al-Cu alloy 2024 irradiated for various number of laser pulses.

3.3. Tensile testing

The stress–strain curves of (a) un-irradiated and laser irradiated Al-Cu alloy 2024 for various number of laser pulses of (b) 750 (c) 1500 (d) 2250 (e) 3000 (f) 3750 are shown in figure 5.

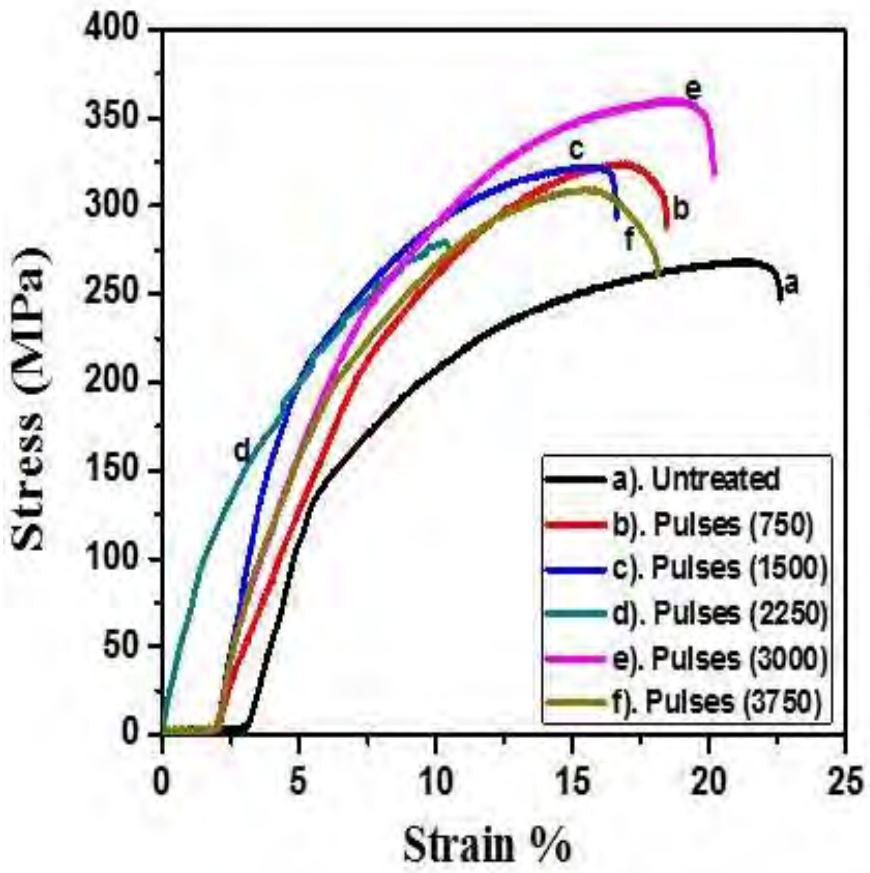

Figure 5: The stress-strain curves of (a) unirradiated and laser irradiated Al-Cu alloy 2024 for various number of laser pulses of (b) 750 (c) 1500 (d) 2250 (e) 3000 and (f) 3750.

The variations in mechanical behavior of the metal alloy such as changes in Yield Strength (YS) and Ultimate Tensile Strength (UTS) for various number of laser pulses are plotted in figure 6 and 7.

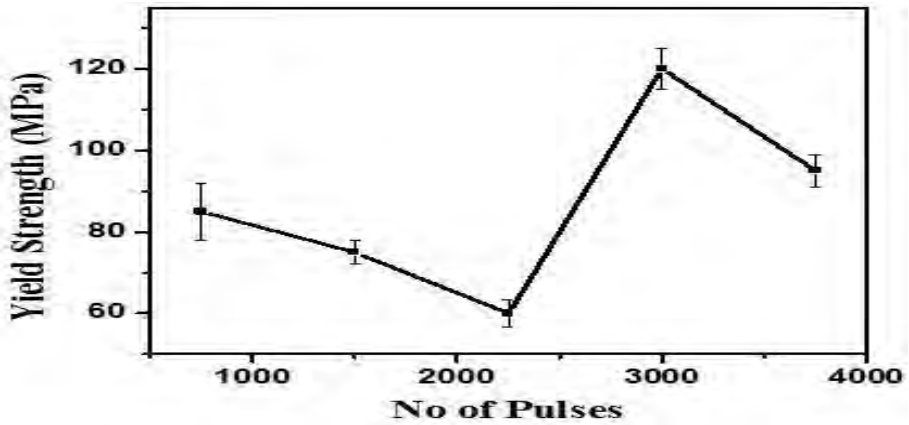

Figure 6: The variation of yield stress of irradiated Al-Cu alloy 2024 for various number of laser pulses.

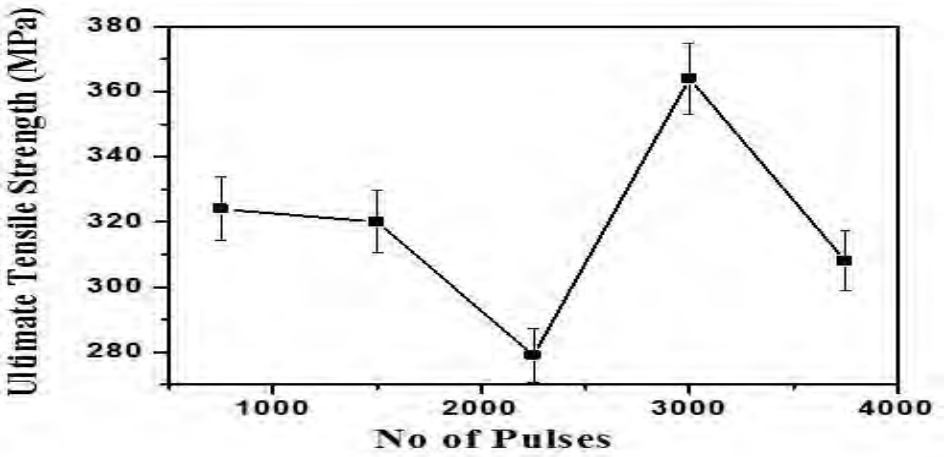

Figure 7: The variation of ultimate tensile stress of irradiated Al-Cu alloy 2024 for various number of laser pulses.

These variations in the values of mechanical properties (YS and UTS) of Al-Cu alloy can be attributed to the alterations in microstructure explored by SEM analysis and dislocation density explored by XRD analysis which is produced by laser beam-material interactions.

However, the values of YS and UTS of the sample initially decrease after laser irradiation for laser pulses from 750 to 2250 as compared to untreated sample. However, an increase in the values of YS & UTS is observed when the laser pulses are increased from 2250 to 3000. Again a decreasing trend in YS & UTS is observed for the highest number of laser pulses of 3750.

When laser pulses are increased from 750 to 2250, localized heating increases, due to which defects density and residual stresses are decreased. The reduction in residual stresses causes decrease in tensile strength of the material. Consequently, YS and UTS decreases. When laser pulses are increased from 2250 to 3000, YS & UTS increases. The laser induced defects, stresses and strain field are possible reason for increasing behavior of YS and UTS with increasing laser pulses. The improvements of hardness of exposed targets in comparison to unexposed target are also correlated with the generation of the dislocation density, grain size and the microstructural deformation near the surface [29].

When laser pulses are increased up to the maximum value of 3750, the more heating and cooling of the material takes place which causes annealing and is responsible for the reduction of defect-density. The reduced density of defects causes the decrease in the tensile strength [30]. Therefore, for the maximum laser pulses of 3750, the tensile strength decreases. Hence, the anomalous behaviors of tensile properties of Al-Cu alloy 2024 for various number of laser pulses is mainly due to grain refinement, generation and variation in defects density.

3.4. Micro hardness

Figure 8 shows the variation in the value of the microhardness from 76 HV to 83 HV for different number of laser pulses ranging from 750 to 3750. It is observed that microhardness of irradiated samples increases as compared to microhardness of untreated sample that is 63 HV. The microhardness initially decreases for increasing laser pulses from 750 to 2250. An increase in the microhardness is observed when the laser pulses are increased from 2250 to 3000. At a maximum number of laser pulses of 3750, a significant reduction in the microhardness of the irradiated material

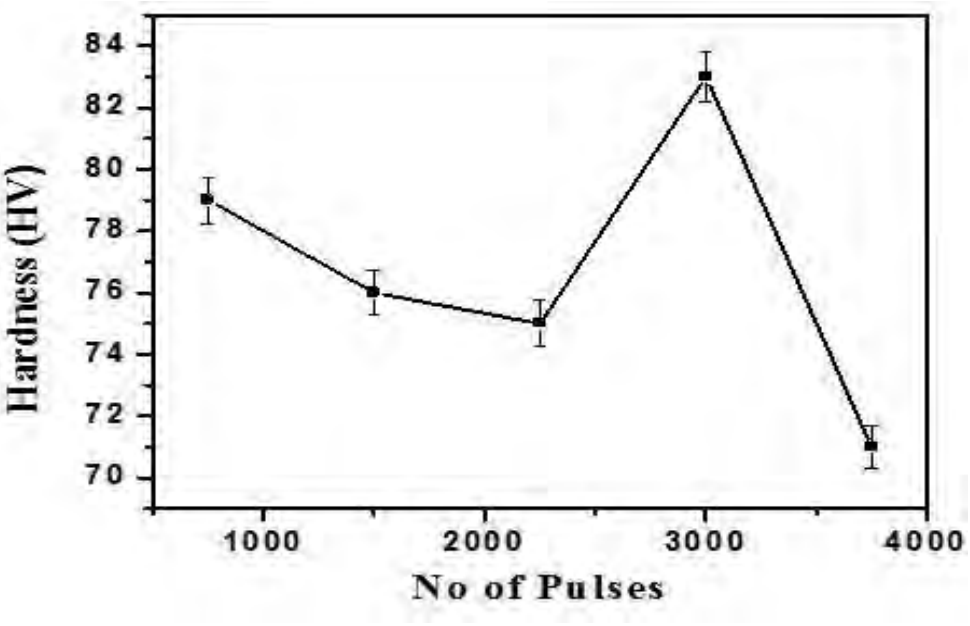

is observed.

Figure 8: The variation of the microhardness of irradiated Al-Cu alloy 2024 for various number of laser pulses.

The changes in microhardness are attributed to the lattice disorder and are associated with changes in crystal structure and thermal compressive stresses produced in the material as the result of laser induced heating [28]. The change in microhardness can also be correlated with the change in dislocation density and crystal size as has been evaluated by XRD analysis shown in figure 4 & 5. By decreasing grain size and increasing dislocation density, microhardness increases and vice versa [31]. This mechanical response of the material can be correlated with the surface and structural modification of the material. Initially, by increasing the laser pulses from 750 to 2250 due to enhanced energy deposition, heating, melting and boiling of the material take place and craters are formed which cause softness in material and hence tensile strength and hardness decrease. The defect-generation is compensated by the defect-annihilation and consequently material annealing takes place which also causes the softening of the material. When the laser pulses are increased from 2250 to 3000, due to more energy deposition defect density increases

but the size of the crater decreases due to refilling and resolidification of the material. This causes the material to become harder. At the maximum number of laser pulses of 3750, tensile strength and hardness once again decreased due to intense melting, ablation and due to enhancement of crater size of the material as shown in Figure 1 & 8.

Similarly, peak intensity and crystallite size of the material initially increases for the laser pulses ranging from 750 to 2250 whereas dislocation density decreases and causes reduction of tensile strength and microhardness of the material. The tensile strength and microhardness increases for the laser pulses from 2250 to 3000 as both peak intensity and crystallite size decreases whereas dislocation density increases which acts as a barrier for dislocation loop and therefore, consequently tensile strength and hardness increase for these laser pulses . For the highest number of laser pulses of 3750, tensile strength and microhardness again decreases as the dislocation density decreases while peak intensity and crystallite size of the material again increases. We can interpret the relationship of surface morphology and the microhardness of the material. By increasing laser pulses, enhanced melting and ablation of the material occurs which causes reduction in hardness. At particular number of laser pulses, hardness increases due to refilling, resolidification processes in the material [32].

4. CONCLUSIONS

The surface, structural and mechanical modification of laser irradiated Al-Cu alloy 2024 has been investigated. SEM results reveal the appearance of crater- formation with laser induced periodic surface structures or multiple ablative layers. By increasing number of laser pulses, the size of the craters initially increases then decreases and ultimately increases revealing anomalous behavior. From YS, UTS, microhardness and XRD results, it is observed that with increase in number of laser pulses, tensile behavior, microhardness, peak intensity, crystalline size and dislocation density of irradiated target also exhibit anomalous behavior. The observed changes in the mechanical properties are well correlated with surface and structural modification of irradiated sample.

ACKNOWLEDGEMENTS

Authors are thankful to Higher Education Commission (HEC) for providing laser facility at Center for Advanced Studies in Physics and Shafqat Ali for providing the SEM facility. We are also grateful to Mr. Sajjad, Miss Uzma Akhlaq and Mr. Ali Husnain who helped us in Tensile Testing and XRD Analysis.

REFERENCES

1. J. F. Ready, "Effect of high-power laser radiation", london, (1971), New York.
2. S. Trusso, L. Torrisi, G. D. Marco and P. Parisi, Physica Medica. XVII, 4 (2001) 849.
3. J. R. Huber and P.R. Willmott, Rev. Mod. Phys., 72 (2000) 162.
4. G. K. Hubler D.B. Chrisey, D. B. Chrisey and G.K. Hubler, "Pulsed Laser Deposition of Thin Films", (1994), New York.
5. D. M. Otterloo and J. L. Hosson, Scrip. Metall. Mater,. 30 (1994) 493.
6. W. Perrie, J. Cheng, G. Dearden and K. G. Watkins, Appl. Surf. Sci., 256 (2009) 1514.
7. K. Dou, E. T. Knobbe, R. L. Parkhill, and Y. Wang, J. Quant. Electro. 6 (2000) 689.
8. A. H Clauer, and B. P. Fairand, "Interaction of laser induced stress-waves with metals", ASM Int. mater. Park OH- 44073 (1979) 22.
9. D. Yousaf, S. Bashir, U. kalsoom and N. Ali, Radi. Effec. & Defec.Solids., 1 (2013) 15.
10. D. B. Chrisey, and G. K. Hubler, "Pulsed laser deposition of thin Film", (1994), New York.
11. J. Badziak, E. Woryna, P. Parys, R. Suchañska, K. Rohlena, Nukleonika, 47 (2002) 147.
12. C. Koner, V. Hartmann, and H.W. Bergmann. J. Appl. Phys. A., 63 (1996) 123.
13. A. Dauscher, V. Feregotto, P. Cordier, and A. Thomy, Appl. Surf. Sci., 410 (1996) 96.
14. M. Huang, Y. Cheng, N. Xu, and Z. Z. Xu, ACS. Nano., 3 (2009) 4062.
15. Y. F. Lu and J. J. Yu, Appl. Surf. Sci., 148 (1999) 248.
16. H. G. Rubahn, "Laser applications in surface science and technology", (1999).
17. B. N. Chichkov, F. V. Alvensleben and A. Tunnermann, J. Appl. Phys. A., 63 (1996) 109.
18. B. P. Fairand, A. H. Clauer, and B. A. Wilcox, Met.Trans. A., 8 (1977) 1871.
19. S. Z. Kubair, D. Evans, A. G, Clarke and V. Tolpygo, Acta. Mater. 51 (2003) 959.
20. D. Pranav, L. Gaoren, J. H. Li and R.Y. Lin. Tsing. Sci. Techn., 10 (2005) 690.
21. R. Ahmad, U. Kalsoom, N. Ali, and N. Khan, Plasma Sci. & Technol., 15 (2013) 666.
22. B. D. Cullity, "Elements of X-rays diffraction". (1978), London.
23. N. Ali, S. Bashir, M. Akram and K. Mahmood, Appl. Surf. Sci. 270 (2013) 49.
24. M. K. Rehman, M. S. Rafique and K. A. Bhatti, Physica B., 406 (2011) 1713.
25. B. D. Cullity and S.R. Stock, "Elements of X-ray diffraction". 3 (2001), London.
26. S. Venkatachalam, K. Kim, and Y. Junsin, Sol. Elect., 48 (2004) 2219.
27. S. Bashir, U. Kalsoom and N. Ali, Surf. Coat. & Technol. 235 (2013) 297.
28. W. F. Smith, "Principles of material sciences and engineering", (1990), Tokyo.

29. P. Peyre, R. Fabbro, P. Merrien, and H. P. Lieurade, Mat. Sci. Eng. A., 210 (1996) 102.
30. J. Fourier, Mat. Manufac. Proc., 5 (1990) 144.
31. J. Fournier, "Modern mechanical surface treatment, states, stability", dissertation, (1989).
32. D. Shi and G. Huang, ISIJ. International., 52 (2012) 1888.

JOURNAL OF NATURAL SCIENCES AND MATHEMATICS
INFORMATION FOR AUTHORS

1. TYPES OF PAPERS ACCEPTED

The Journal aims at publishing original research papers and the review papers from distinguished scientists on Mathematics, Physics, Chemistry and Computer Science.

2. SUBMISSION OF MANUSCRIPTS

Manuscripts should be submitted in MS Word format through e-mail to the relevant editor. All papers are refereed. The decision of the Editorial Board regarding the acceptance and publication of the paper will be final.

3. PREPARATION OF MANUSCRIPT

3.1 Language and Style

All submissions should be in English; typed in double spacing on one side of the paper only with a left hand margin of at least 4 cm. Mathematical expressions must be carefully printed. Computer composed manuscript on C.D. or through e-mail in MS Word format is required for speedy publication.

3.2 Abstract

This should comprise a brief and factual summary of contents and should be suitable for direct use by abstracting journals. This will seldom require more than 200 words.

3.3 Section/Sub-Section Headings

Papers should be divided into sections / sub-sections and numbered as exemplified in the headings of this INFORMATION FOR AUTHORS.

3.4 References

References should be numbered consecutively in the text, e.g. “According to a recent theory [6]…it is well established [7]” and collected at the end of the paper in following style:

6. I. M. Ghauri and P. Feltham, J. Nat. Sci. Math., 26 (1986) 63.

7. W. Greiner and J. Maruhn, Nuclear Models, Springer-Verlag, Berlin, (1996).

3.5 Illustrations

Line diagrams must be drawn in black ink on white paper; original and two copies are required. Photographs or half-tone reproduction should be in the form of highly glazed prints. Figures are also acceptable in the form of jpg or tif format of 300 dpi. A separate list of captions for illustrations should be provided.

4. PROOFS

Only one set of proof is sent to the authors for correction.